RESEARCH ARTICLE

Eruption of compositionally heterogeneous andesites from a complex storage region during the 2006 eruption of Augustine Volcano

Mary C. Benage[1] · Heather M. N. Wright[1] · Michelle L. Coombs[2]

Abstract

Despite the common occurrence of heterogeneous andesitic eruptions, few studies have investigated the compositional effects on microlite crystallization and vesiculation in co-erupted natural samples. In 2006, Augustine Volcano erupted compositionally heterogeneous andesites that range from 56.4 to 63.3 wt% SiO_2 and include two endmember lithologic groups: low-silica andesite (LSA) and high-silica andesite (HSA). Textural and compositional differences between LSA and HSA end members are explored for two discrete, sequential vulcanian explosions from January 17 (event 9) and 27 (event 10), 2006. Groundmass glass compositions of pyroclasts within LSA and HSA compositional suites are not colinear and do not correlate with plagioclase microlite crystallinities, indicating eruption from multiple isolated shallow magma reservoirs with various pressure-temperature pathways. HSA pyroclasts have lower crystallinities, 0.02–0.24, than most LSA pyroclasts, 0.16–0.39, demonstrating the influence of composition on crystallinity. Additionally, microlite textural and groundmass glass compositional differences exist between consecutive vulcanian explosions. The event 9 deposits have a typical bimodal density distribution and groundmass glass compositions range from 65 to 78 wt% SiO_2. Plagioclase microlite number densities (MN_V) are $10^{4.6–6.4}$ mm^{-3} and crystallinities are 0.02 to 0.28, similar to products from other andesitic vulcanian eruptions. Deposits from the early phase of event 10 have a bimodal density distribution and contain a high proportion of LSA pyroclasts, similar to event 9. Groundmass glass compositions range from 72 to 79 wt% SiO_2 and plagioclase MN_V are $10^{5.9–6.3}$ mm^{-3}, forming narrower ranges compared to event 9. A transition occurred during the later phase of event 10 to a unimodal density distribution, a more homogeneous groundmass glass composition, 75–78 wt% SiO_2, a higher proportion of HSA pyroclasts, and the highest MN_V of $10^{5.9–6.7}$ mm^{-3}. We interpret this shift to reflect eruption from reservoir depths around 4–6 km and the cessation of pre-eruptive magma staging in the upper conduit, transitioning the eruption to continuous and effusive phases. Attention to heterogeneous andesitic erupted products reveals additional details about heterogeneous shallow magma storage, variable upper conduit magma staging, and a range of pressure-temperature paths prior to fragmentation.

Keywords Andesite · Vulcanian · Microlite · Vesicle · Augustine · Magma decompression path

✉ Mary C. Benage
mbenage@usgs.gov

1 U.S. Geological Survey, Cascades Volcano Observatory, Vancouver, WA 98683, USA

2 U.S. Geological Survey, Alaska Volcano Observatory, Anchorage, AK 99508, USA

Introduction

The textures of volcanic pyroclasts reflect complex histories of crystallization and vesiculation prior to and during magma ascent. Insight into the plumbing of the shallow magma system and history of magma ascent can be derived from groundmass glass compositions and crystal and vesicle textures of erupted pyroclasts as they respond to pressure, temperature, and composition changes in the system (e.g., Bain et al. 2019; Cashman 2004; Cassidy et al. 2015; Edmonds and Woods

2018; Giachetti et al. 2010; Shea et al. 2010; Swallow et al. 2018). Furthermore, microlite and vesicle textures record different stages of magma decompression and ascent because of differences in the kinetics of crystal and bubble nucleation and growth and the ability for bubbles to migrate out of the system. Microlite number densities (MN_V) vary with decompression path and/or pre-eruptive equilibration depth (e.g., Befus and Andrews 2018; Cashman and McConnell 2005; Hammer et al. 1999; Hammer and Rutherford 2002; Klug and Cashman 1994; Shea et al. 2010; Toramaru et al. 2008) and duration of shallow storage (i.e., interevent repose time; Hammer et al. 2000). That is, microlite textures and phenocryst rim growth (Befus and Andrews 2018; Riker et al. 2015) record both pre-eruptive, or magma staging decompression, and syn-eruptive decompression paths. Vesicle textures also preserve information about pre-eruptive (Toramaru 2014) and syn-eruptive ascent, where small vesicles are attributed to syn-eruptive ascent of magma in the conduit and late-stage conduit processes (Klug et al. 2002; Klug and Cashman 1994; Mangan et al. 1993). Furthermore, vesicle number densities (VN_V) can be used to estimate syn-eruptive magma decompression rates, if bubble nucleation is homogeneous (Cluzel et al. 2008; Toramaru 2006). Eruption explosivity and eruption style are intimately linked (e.g., Blundy and Cashman 2005; Cassidy et al. 2018; Degruyter et al. 2012; Jaupart and Allegre 1991; Melnik and Sparks 1999; Sparks 1997; Woods and Koyaguchi 1994) to the complex feedback loop of magma ascent, degassing, crystallization, and melt compositional evolution (Cashman 2004; Couch et al. 2003; Hammer et al. 1999, 2000; Kirkpatrick 1981; Sparks 1997). By combining groundmass glass composition and vesicle and microlite textural information, we can learn more about the shallow magma storage and ascent, which strongly control eruption style.

Past textural studies of eruptive products document variations in microlite and vesicle size, shape, and abundance that are attributed to differences in pressure/temperature pathways (e.g., Cashman 2004; Gardner et al. 1998; Hammer et al. 1999; Taddeucci et al. 2004; Wright et al. 2012), where bulk composition is held constant. However, subtle compositional heterogeneity is found in the intermediate-composition eruptive products of many stratovolcanoes, especially those produced during single short-lived explosions (e.g., Trident (Coombs et al. 2000), Augustine (Larsen et al. 2010; Roman et al. 2006), Redoubt (Coombs et al. 2013; Wolf and Eichelberger 1997), Ruapehu (Pardo et al. 2014), and Soufrière Hills (Humphreys et al. 2010)).

Despite the occurrence of modest compositional heterogeneity, its effects on microlite crystallization and vesiculation during decompression have not been previously investigated in detail on a suite of co-erupted natural samples. Here, we focus on explosive eruptive deposits that span the andesitic compositional field from two sequential vulcanian explosions of the 2006 eruption of Augustine Volcano. We use variations in componentry, groundmass glass and plagioclase compositions, temperature and oxygen fugacity from Fe-Ti oxide pairs, vesicle number density (VN_V), and plagioclase microlite number density (MN_V) and crystallinity (ϕ) to answer two questions: (1) how do pyroclast characteristics vary between low-silica and high-silica andesites erupted during the same explosive event? and (2) for two sequential explosions, can we use variations in textures and compositions to better understand magma decompression, shallow magma storage, and changes in the magmatic system that affect eruption explosivity and style? We show that small changes in andesite whole-rock and accompanying melt SiO_2 content result in variations in pyroclast density, vesicle number density, and microlite content, even among pyroclasts from a single deposit. At Augustine, this compositional diversity provides evidence for spatially discrete shallow magma storage prior to eruption, and we use our data to investigate the complex decompression pathways of co-erupted magma from this network of storage regions.

The 2006 eruption of Augustine Volcano

Augustine Volcano is located in Alaska's Cook Inlet and is part of the eastern Aleutian volcanic arc (Fig. 1). The volcano comprises a summit dome complex surrounded by an apron of pyroclastic density current (PDC) and debris-avalanche deposits (Waitt and Beget 2009). Augustine's historical eruptions in 1883, 1935, 1964, 1976, 1986, and 2006 each produced andesitic to dacitic fall deposits, PDCs, and lava domes (Larsen et al. 2010; Roman et al. 2006; Waitt and Begét 2009).

\The 2006 eruption was documented through observation flights, remote automated camera imagery, and satellite images during the eruption sequence, which allowed for distinction between individual deposits (Coombs et al. 2010; Larsen et al. 2010; Vallance et al. 2010; Wallace et al. 2010). Post-eruption sampling (e.g., Coombs et al. 2010; Vallance et al. 2010; Wallace et al. 2010) and whole-rock analysis (Larsen et al. 2010) revealed that deposits consisted of four dominant lithologies:

1) Low-silica andesite (LSA): whole-rock compositions are between 56.4 and 59.3 wt% SiO_2 (Larsen et al. 2010) and LSA includes two pyroclast subtypes, scoriaceous and dense. LSA scoria pyroclasts are moderately vesicular and occur in various shades of brownish-gray-olive green. Dense LSA pyroclasts are glassy, angular, and medium to light gray (Vallance et al. 2010; Wallace et al. 2010).

2) High-silica andesite (HSA): whole-rock compositions are between 62.2 and 63.3 wt% SiO_2 (Larsen et al. 2010) and HSA pyroclasts are moderately to highly vesicular and light gray (rarely white), pink, to salt-and-pepper in color (Vallance et al. 2010; Wallace et al. 2010).

3) Intermediate andesite: whole-rock compositions are from 58.3 to 62.2 wt% SiO_2 (Larsen et al. 2010) and intermediate andesite pyroclasts are dense, medium gray in color, poorly to non-vesicular (Vallance et al. 2010; Wallace et al. 2010).

4) Banded andesite: whole-rock compositions are from 57.3 to 62.2 wt% SiO_2 (Larsen et al. 2010) and banded pyroclasts are a combination of the above with distinct to diffuse banding (Vallance et al. 2010; Wallace et al. 2010).

Each lithology is present in each deposit type throughout the entire eruptive sequence, but componentry varies temporally and spatially among deposits (Fig. 2; Coombs et al. 2010; Vallance et al. 2010).

The 2006 eruption is separated into three distinct eruptive phases (Fig. 2; Power et al. 2006), similar in progression to other historical eruptions of Augustine Volcano (e.g., 1976, 1986; Roman et al. 2006; Waitt and Begét 2009). Phases are distinguished by variations in eruptive style, componentry of eruptive products (Coombs et al. 2010; Vallance et al. 2010; Wallace et al. 2010), and by corresponding deformation of the edifice (Cervelli et al. 2010).

Following several weeks of unrest, the explosive phase of the 2006 eruption began on January 11, 2006, lasted 17 days (January 11–28, 2006), and included 13 discrete explosions (events 1–13). The explosive phase began with two discrete explosions (events 1–2) on January 11 that produced snow-
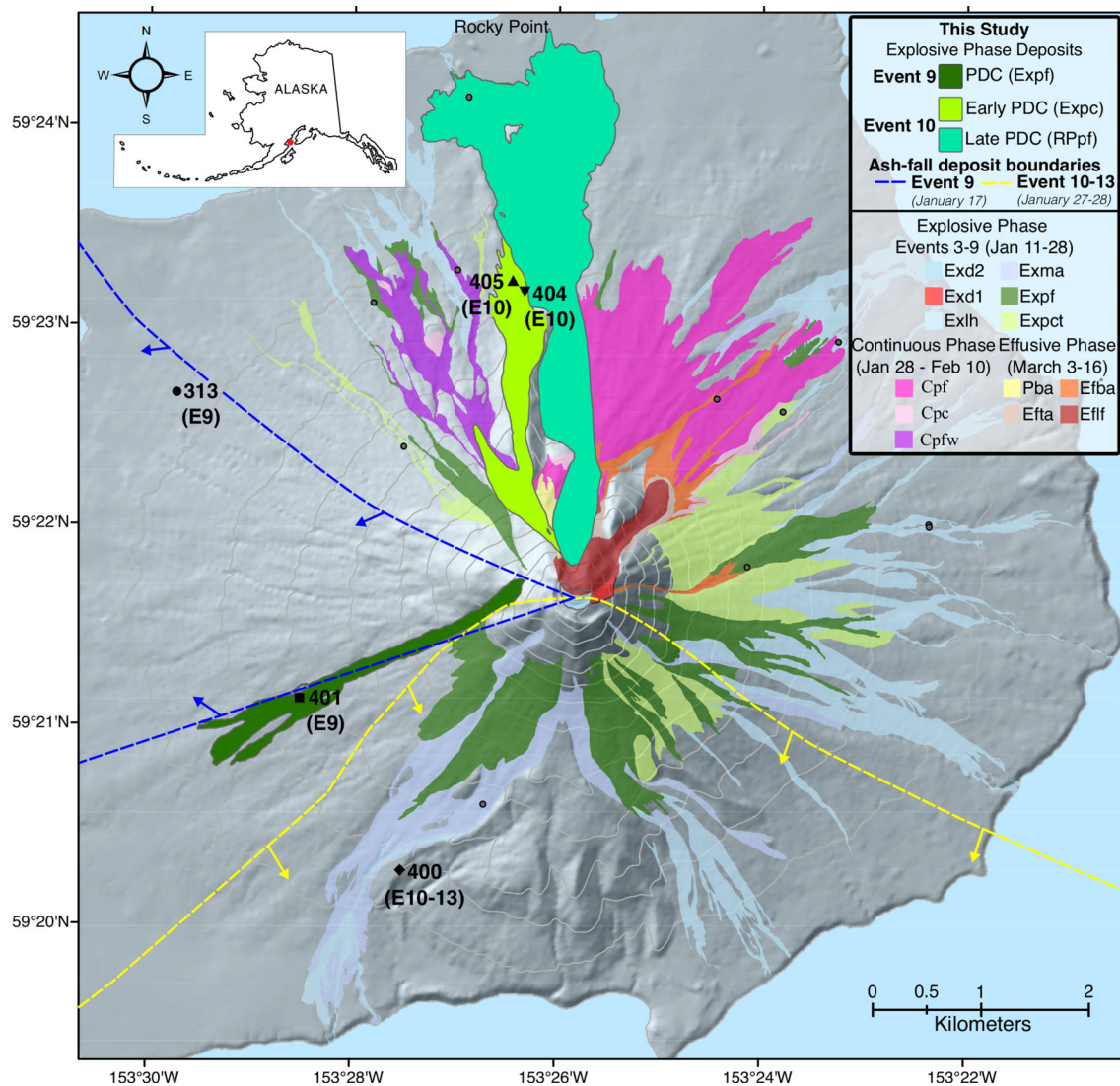
Fig. 1 Distribution of eruptive deposits from the 2006 Augustine eruption (modified from Coombs et al. 2010 and Wallace et al. 2010). Inset map of Alaska shows Augustine's location, a red dot, in the Cook Inlet of the eastern Aleutian volcanic arc. Sample locations for textural and geochemical analyses in this paper are shown with large symbols and labeled by sample number and event number (e.g., 313 (E9)). Small circles represent sample locations for which additional density and componentry analyses were completed. Note that deposits of events 9 and 10 are plotted on top of the map but in reality these deposit areas lie below the continuous and effusive phase units. Blue and yellow dashed lines and arrows indicate the deposit boundary and direction of ash-fall for explosive events 9 and 10–13, respectively (Wallace et al. 2010). See Vallance et al. (2010) for a complete description of the depositional units

Fig. 2 From 14 of the 17 sample locations, lithologic components (by mass) of the four main lapilli-size pyroclast types, low-silica andesite (LSA), intermediate andesite, banded andesite, and high-silica andesite (HSA), versus phase of eruption. Low-silica andesite is subdivided into two pyroclast types: dense (dense LSA) and scoria (LSA scoria). Augustine Volcano 2006 eruption begins with an explosive phase (events 1–13) and ends with an effusive phase. The timeline of the 2006 Augustine eruption (modified from Coombs et al. 2010) shows the 13 discrete explosive events (vertical lines) of the explosive phase, with events 9 and 10 highlighted in black; they are the focus of this study
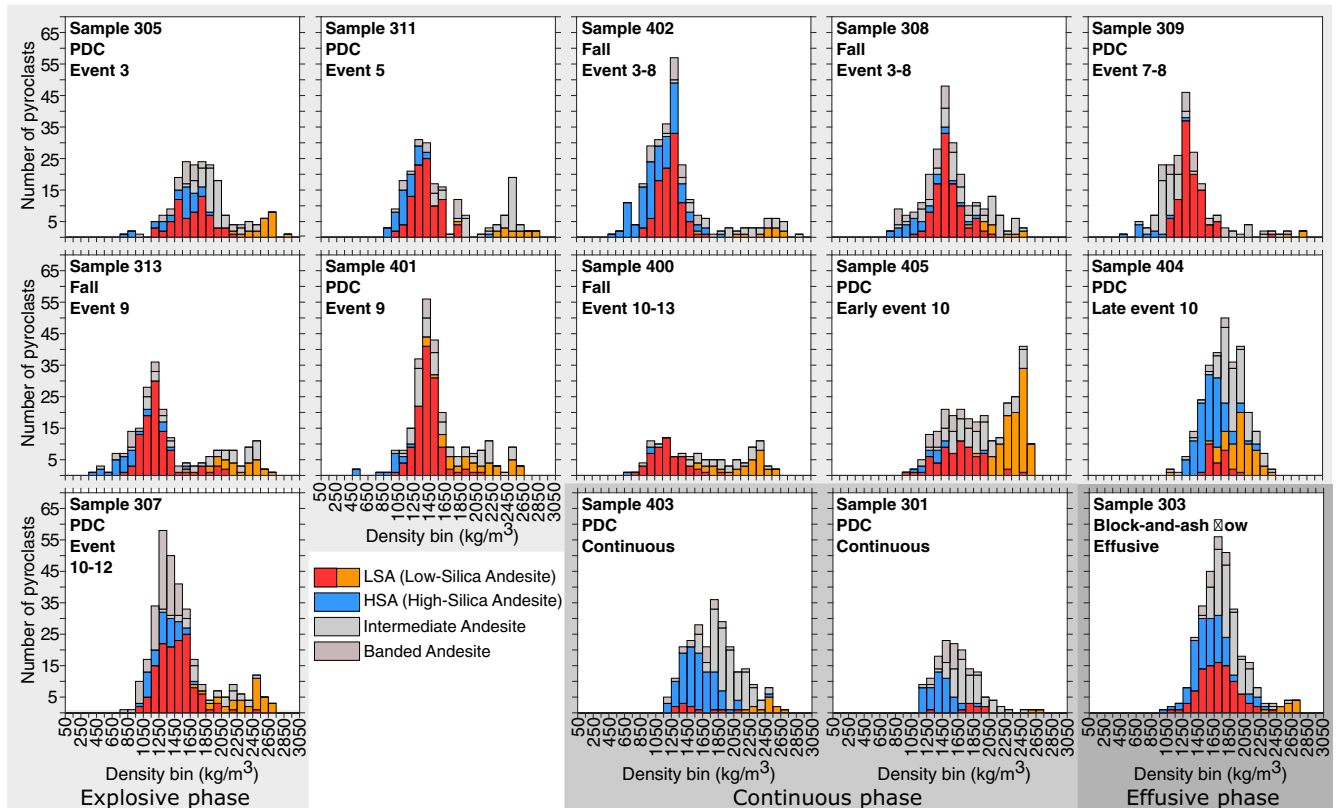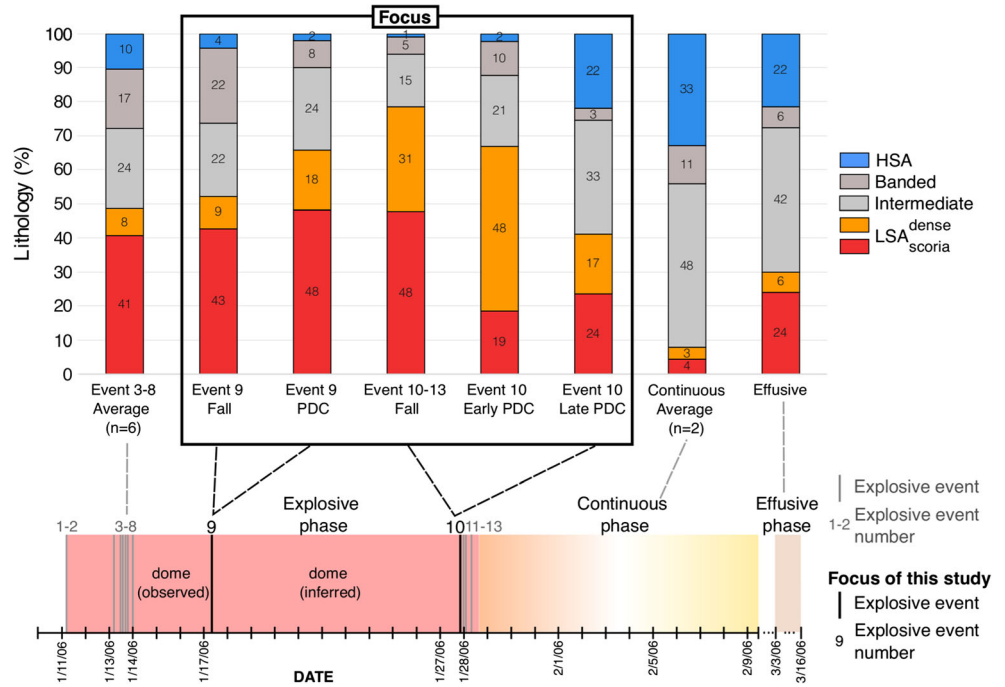
Fig. 3 Density histogram of 16–32 mm pyroclasts by lithologic components, sample location, and sample type for 14 of the 17 sample locations (see Table S1 in supplementary information; not plotted are samples 312, 300, and 406). Explosive phase pyroclasts have a weak to strong bimodal density distribution. Late event 10 (from explosive phase) PDC, continuous, and effusive phase pyroclasts have a unimodal density distribution

rich avalanches. On January 13–14, a series of six explosions (events 3–8) produced PDCs that traveled down the north, east, and south flanks of the volcano (Fig. 1). Between January 14 and 17, a LSA lava dome formed in the eastern half of the summit crater (Coombs et al. 2010).

On January 17, event 9 erupted through the LSA lava dome. The resulting PDC left a deposit rich in dense LSA on the southwest flank and the tephra fall deposits are distributed to the west (Fig. 1; Coombs et al. 2010; Vallance et al. 2010; Wallace et al. 2010). After event 9, a HSA lava dome is inferred to have effused from January 17 to 27 (Coombs et al. 2010; Larsen et al. 2010).

On January 27, explosive event 10 generated two PDCs. The event began with an early phase PDC that left a deposit rich in dense LSA pyroclasts on the north-northwest flank. A later phase of event 10 generated the largest volume PDC, named the Rocky Point pyroclastic flow (RPpf), that swept down the north flank with a 4.7-km runout distance (Fig. 1; Coombs et al. 2010; Vallance et al. 2010). The second PDC is more HSA dominant than the earlier PDC of event 10. This increase in HSA marked a transition in eruption style from intermittent explosions to a subsequent continuous phase, which was more HSA-dominant (Coombs et al. 2010). Following event 10, three short explosive events (events 11–13) on January 27 and 28 produced unidentified but likely minor on-island deposits. A cumulative tephra fall deposit from events 10–13 lies to the south (Fig. 1; Wallace et al. 2010).

Following the intermittent explosive phase characterized by vulcanian activity, the continuous phase of the eruption, January 28 through February 10, began with 4 days of nearly continuous block-and-ash flows to the north and northeast of the summit. The magma flux waned around February 2 and lava flow effusion lasted from February 2 to 10. Following a 23-day hiatus, the effusive phase began on March 3 with lava effusion and frequent but small block-and-ash flows. Active lava effusion ended around March 16, thus concluding the 2006 Augustine eruption (Coombs et al. 2010).

Methods

Sample collection for componentry and density measurements

In 2010, from 17 sites, we collected samples from deposits of the explosive to effusive phases of the 2006 Augustine eruption for componentry and density measurements (Figs. 1 and 2; Table S1 in supplementary information). PDC deposit samples were sieved in the field to select the 16–32 mm (lapilli) size range. For fall deposits, which are typically finer grained than PDC deposits, we hand-picked larger lapilli-size pyroclasts from the deposits. Sorted lapilli-size samples were rinsed under tap water to remove adhering matrix.

For each of the 17 samples, following the criteria of Vallance et al. (2010) and Wallace et al. (2010), the lapilli-size pyroclasts were visually sorted into one of the four lithologic components (LSA, HSA, intermediate andesite, or banded andesite). Low-silica andesite was further subdivided into scoria (LSA scoria) and dense (dense LSA) lapilli. For the remainder of the paper, we refer to the lapilli as pyroclasts.

We measured the density of 4112 pyroclasts in total for all lithological components from the 17 samples (Table S1 in supplementary information) using the density method based on Archimedes principle (Houghton and Wilson 1989). Within each lithologic component for a given sample, density measurements were made for all pyroclasts (for samples with < 100 pyroclasts in that component) or 100 pyroclasts (for samples with > 100 pyroclasts in that component; Fig. 3 and Table S1 in supplementary information).

Sample selection for textural and compositional analysis

In this study, we focus on five samples (three PDC and two tephra fall) relating to events 9 and 10 (see Fig. 1; Table 1) for textural and compositional analysis. Event 9 and 10 explosions both occurred in the presence of a pre-existing dome, are two of the larger vulcanian explosions, and produced distinguishable deposits formed, for the most part, by single explosions. The three PDC samples we examined include event 9 PDC (sample 401), early event 10 PDC (sample 405), and late event 10 PDC (sample 404; samples correspond to Expf, Expc, and RPpf, respectively; see Vallance et al. (2010) for more details). The two tephra fall samples represent event 9 (sample 313) and events 10–13 (sample 400). Sample 400 is likely dominated by event 10 compared to events 11–13 products based on the relatively longer seismic signal duration, airborne ash recorded from radar, and the largest measured lightning flashes of event 10 (Coombs et al. 2010; McNutt et al. 2010; Thomas et al. 2010). Pyroclasts from these five samples were selected from the compositional endmembers, LSA and HSA (Table 1), in order to characterize vesicle and plagioclase microlite textures and groundmass glass and plagioclase composition.

We selected pyroclasts for detailed study based upon measured clast density (cf. Shea et al. 2010). We assume that density modes provide information about the dominant eruptive processes of each compositional endmember, and density tails preserve information about end-member processes (Fig. 4). Throughout this paper, unless otherwise distinguished as density tails, samples are from the mode of the density distribution for each event. For the 30 selected pyroclasts (including density tails of LSA scoria and HSA for event 9), plagioclase microlite texture and groundmass glass composition were analyzed. Of these, eight pyroclasts were also analyzed for plagioclase and Fe-Ti oxide

Table 1   List of samples, sample type, explosion date, and corresponding geochemical and textural data

Site name	Pyroclast name	Type	Lithology	Density type	Density [kg/m³]	Explosive event	Deposit type	Explosion date	Repose time [days]	Range of groundmass glass SiO2 wt% (number of point analyses)	An range for microlite and phenocryst plagioclase (number of point analyses)	N (number oxide pairs)	Fe-Ti oxide temperature†
313	LSAS3	Scoria	LSA	Low-tail	1000	9	Fall	January 17, 2006	3	74.06–75.08 (15)	–	–	
313	LSAS7	Scoria	LSA	Mode	1180	9	Fall	January 17, 2006	3	64.63–66.04 (15)	–	–	
313	LSAS4*	Scoria	LSA	Mode	1250	9	Fall	January 17, 2006	3	65.35–67.78 (7)	48–83 (18)	6	
313	LSAS15	Scoria	LSA	High-tail	1380	9	Fall	January 17, 2006	3	70.69–772.01 (12)	–	–	
313	DLSA8	Dense	LSA	Mode	2520	9	Fall	January 17, 2006	3	74.71–76.67 (14)	–	–	
313	HSA1	Pumice	HSA	Low-tail	520	9	Fall	January 17, 2006	3	75.53–76.40 (15)	–	–	
313	HSA4	Pumice	HSA	Mode	760	9	Fall	January 17, 2006	3	72.85–73.90 (11)	–	–	
313	HSA6	Pumice	HSA	Mode	790	9	Fall	January 17, 2006	3	75.25–75.86 (10)	–	–	
313	HSA9	Pumice	HSA	Mode	870	9	Fall	January 17, 2006	3	74.31–75.31 (11)	–	–	
313	HSA3*	Pumice	HSA	Mode	880	9	Fall	January 17, 2006	3	76.92–78.29 (8)	46–74 (18)	4	
313	HSA5	Pumice	HSA	High-tail	1300	9	Fall	January 17, 2006	3	76.24–77.10 (14)	–	–	
401	LSAS30	Scoria	LSA	Low-tail	1180	9	PDC	January 17, 2006	3	68.07–73.15 (14)	–	–	
401	LSAS9**	Scoria	LSA	Mode	1400	9	PDC	January 17, 2006	3	69.45–70.79 (9)* 69.16–70.33 (11)	48–64 (12)	10	
401	LSAS6	Scoria	LSA	Mode	1400	9	PDC	January 17, 2006	3	66.34–67.57 (15)	–	–	
401	LSAS13	Dense	LSA	High-tail	1550	9	PDC	January 17, 2006	3	66.04–67.50 (10)	–	–	
401	DLSA18	Dense	LSA	Mode	2170	9	PDC	January 17, 2006	3	75.80–77.67 (14)	–	–	
401	HSA7	Pumice	HSA	Low-tail	500	9	PDC	January 17, 2006	3	75.52–75.986 (12)	–	–	
401	HSA3*	Pumice	HSA	Mode	1010	9	PDC	January 17, 2006	3	72.25–76.59 (4)	47–79 (17)	–	
401	HSA1	Pumice	HSA	Mode	1040	9	PDC	January 17, 2006	3	75.17 (1)	–	–	
401	HSA5	Pumice	HSA	High-tail	1120	9	PDC	January 17, 2006	3	73.21–74.44 (12)	–	–	
400	LSAS5*	Scoria	LSA	Mode	1200	10-13	Fall	January 27–28, 2006	10	71.92–72.80 (7)	50–81 (16)	7	
400	DLSA6	Dense	LSA	Mode	2430	10-13	Fall	January 27–28, 2007	10	–	–	–	
400	HSA2*	Pumice	HSA	Mode	1000	10-13	Fall	January 27–28, 2008	10	78.20–78.88 (4)	20–81 (14)	8	
405	LSAS6*	Scoria	LSA	Mode	1700	10	Early PDC	January 27, 2006	10	73.09–76.06 (7)	49–70 (18)	3	
405	DLSA12	Dense	LSA	Mode	2480	10	Early PDC	January 27, 2006	10	73.44–74.97 (13)	–	–	
405	HSA3*	Pumice	HSA	Mode Mode	1440	10	Early PDC	January 27, 2006	10	78.19–79.33 (7)	41–76 (17)	–	
404	LSAS2	Scoria	LSA	Mode	1590	10	Late PDC	January 27, 2006	10	75.16–76.78 (16)	–	–	
404	DLSA18	Dense	LSA	Mode	2010	10	Late PDC	January 27, 2006	10	75.32–77.99 (15)	–	–	
404	HSA5	Pumice	HSA	Mode	1580	10	Late PDC	January 27, 2006	10	74.98–76.03 (15)	–	–	
404	HSA18	Pumice	HSA	Mode	1590	10	Late PDC	January 27, 2006	10	75.01–76.59 (17)	–	–	

Table 1 (continued)

Site name	Pyroclast name	Average and Std temperature [°C]	Avgerage and Std fO_2	N (number of microlites)	MNA [mm^{-2}]	φ microlite crystallinity	log [MNV mm^{-3}]	Number of broken phenocrysts ($N>5$ ††)	N (number of vesicles)	VNV [mm^{-3}]	log [VNV mm^{-3}]	2D ves%
		Fe–Ti oxide temperature†		Plagioclase microlite					Vesicle			
313	LSAS3	–	–	655	4291	0.18	5.83		–	–	–	–
313	LSAS7	–	–	661	2779	0.24	5.48		–	–	–	–
313	LSAS4*	986±62	1.3±0.01	658	4576	0.28	5.77		1267	3.08×10^6	6.49	59.28
313	LSAS15	–	–	861	4123	0.28	5.70		–	–	–	–
313	DLSA8	–	–	1388	11,366	0.23	6.40	27	–	–	–	–
313	HSA1	–	–	57	795	0.01	5.28	\	–	–	–	–
313	HSA4	–	–	264	2712	0.24	5.46		–	–	–	–
313	HSA6	–	–	30	340	0.02	4.66		–	–	–	–
313	HSA9	–	–	290	3086	0.20	5.58		–	–	–	–
313	HSA3*	877±8	1.4±0.03	282	2590	0.04	5.82		2875	1.57×10^7	7.20	75.62
313	HSA5	–	–	894	4409	0.26	5.76		–	–	–	–
401	LSAS30	–	–	882	4188	0.24	5.74		–	–	–	–
401	LSAS9**	1038±13	1.2±0.04	656	3025	0.26	5.52		1033	1.86×10^6	6.27	43.07
401	LSAS6	–	–	1184	3650	0.26	5.63		–	–	–	–
401	LSAS13	–	–	734	4751	0.25	5.82		–	–	–	–
401	DLSA18	–	–	1333	10,243	0.25	6.31	13	–	–	–	–
401	HSA7	–	–	37	526	0.03	4.84		–	–	–	–
401	HSA3*	–	–	53	456	0.06	4.59		1736	4.10×10^6	6.61	66.01
401	HSA1	–	–	775	7049	0.15	6.19		–	–	–	–
401	HSA5	–	–	883	5751	0.35	5.87		–	–	–	–
400	LSAS5*	1024±22	1.0±0.04	961	5160	0.21	5.90	10	–	–	–	–
400	DLSA6	–	–	–	–	–	–	–	–	–	–	–
400	HSA2*	938±13	1.2±0.04	383	5834	0.17	6.03	60	–	–	–	–
405	LSAS6*	1087±38	0.9±0.28	3012	10,544	0.25	6.33	70	–	–	–	–
405	DLSA12	–	–	609	9435	0.39	6.17	6	–	–	–	–
405	HSA3*	–	–	703	4882	0.11	6.01	10	–	–	–	–
404	LSAS2	–	–	1508	15,328	0.16	6.68		–	–	–	–
404	DLSA18	–	–	748	18,075	0.24	6.69		–	–	–	–
404	HSA5	–	–	1023	2961	0.04	5.89		–	–	–	–
404	HSA18	–	–	985	6651	0.11	6.22		–	–	–	–

– not measured

*Groundmass glass, plagioclase, and Fe–Ti oxide pair compositions measured on USGS Denver JEOL JXA-8900 electron microprobe

All other groundmass glass compositions measured on Smithsonian Institute National Museum of Natural History Mineral Sciences Department's JEOL-JXA 8530F electron microprobe

**401LSAS9 groundmass glass composition was analyzed on both electron microprobes

†Temperature and oxygen fugacity calculated with Ghiorso and Evans (2008) geothermometer (exclude temperatures > 1150 °C)

††Number of broken plagioclase counted for all pyroclasts analyzed but only report if the number is greater than 5

composition (event 9 and early event 10). For event 9, we quantified the vesicle texture of four pyroclasts (LSA scoria and HSA; Table 1).

Image acquisition and textures

Vesicle and plagioclase microlite textures were characterized using backscattered electron (BSE) scanning electron microscope (SEM) images. Images were obtained on a desktop ASPEX EXpress SEM at the U.S. Geological Survey (USGS) Cascades Volcano Observatory using a 20-keV electron beam. The working distance was 16–17 mm at × 139–555 magnification or 45–47 mm at × 27 magnification.

Vesicle number density

Vesicle number densities (VN_V) for four event 9 pyroclasts were calculated using FOAMs software (Shea et al. 2010). For each pyroclast, the collected BSE images were comprised of an exponential nest of 4 overlapping magnifications that include (1) scan of thin section, (2) 3 BSE images at × 27, (3) 6 BSE images at × 139, and (4) 12 BSE images at × 555 (Shea et al. 2010). These BSE images were used in the FOAMS software to calculate VN_V (Shea et al. 2010). Vesicle diameters range in size from 0.001 to 2 mm. At the lowest magnification images, we hand-traced vesicles and crystals larger than 0.2 mm and at least 10 vesicles were counted to ensure adequate statistical representation (Shea et al. 2010). For higher magnification images, crystals, vesicles, and redrawn broken vesicle walls were digitized by hand (Shea et al. 2010) and a minimum vesicle diameter threshold was set at 10 pixels (Liu et al. 2015; Shea et al. 2010). Vesicle number density, VN_V, values are groundmass-referenced (discarding crystals > 50 μm) and vesicularity-corrected (see Shea et al. 2010 for method details).

Microlite number density

For plagioclase microlite textural characterization, 20 pyroclast thin sections were imaged representing textures from event 9, which include low- and high-density tails, and 10 thin sections of pyroclasts from event 10. The 30 thin sections were imaged either at × 555 with a resolution of 1024 × 1024 pixels or × 280 at a resolution of 2048 × 2048 pixels, resulting in pixel sizes of 0.16 μm. For the × 555 resolution, 9 images were collected and stitched together with 50% overlap using Fiji software (Preibisch et al. 2009; Schindelin et al. 2012) to produce a single image measuring ~ 1700 × 1900 pixels. In order to capture at least 500 microlites per sample (except for microlite-poor HSA samples; Table 1), plagioclase microlites and phenocrysts were hand-traced on 2 to 6 images (images > 1024 pixels) for LSA and 6 images for HSA. For samples 405 and 404, dense LSA thin-sections were digitized on only two

1024 × 1024 pixel images at 0.16 μm/pixel resolution as these samples were microlite rich.

Microlite number density (MN_V) was quantified for plagioclase, the most abundant microlite phase in all samples, although subsidiary mafic microlite phases include pyroxene, trace amphibole, and Fe-Ti oxides. All plagioclase microlites and all phenocryst phases were hand-traced in each of the 2–6 SEM BSE images per pyroclast. The average length of the counted microlites range from a minimum of 1.55 μm, based on the statistical shape inaccuracies at < 10 pixels (Liu et al. 2015; Higgins 2000), to a maximum of 50 μm, based upon visual inspection of plagioclase crystals in the Augustine samples. We define the groundmass as comprising microlites and glass but excluding crystals > 50 μm and vesicles. Plagioclase microlite crystallinity, ϕ, is the fractional area of the groundmass covered by plagioclase microlites, including those cut by the image edge (Hammer et al. 1999; Riker et al. 2015). The number of plagioclase per groundmass area, MN_A, were quantified by counting the hand-digitized microlites that were fully enclosed within each image and those that were cut by the left-hand and upper margin of the image. Using MN_A and ϕ, we calculated the volumetric plagioclase number density $MN_V = (MN_A)/S$, where S is the characteristic crystal size, $S = (\phi /(MN_A))^{0.5}$ (Hammer and Rutherford 2002).

Electron microprobe

Groundmass glass, plagioclase, and oxide pair compositions from eight event 9 and 10 pyroclasts (see Table 1) were analyzed on a JEOL JXA-8900 electron microprobe at a USGS facility in Denver, Colorado. A 15-keV electron beam at 20 nA with a 3- or 5-μm diameter beam was used to analyze matrix glass and plagioclase. Reported compositions are from single spot analyses and secondary standards were used (Table S2 in supplementary information). Alkalis were measured first to avoid significant loss by migration, but minor migration was corrected using a time dependent intensity correction with a log-quadratic (hyper-exponential) fit. Oxide compositions were analyzed with a 15-keV focused electron beam at 20 nA. All analyzed oxide pairs were touching ilmenite-magnetite pairs and analyzed spots lie within 10 μm of the contact.

Groundmass glass compositions of the remaining 22 pyroclasts from the 5 samples (includes event 9 density tails and additional density modes) were analyzed on the JEOL-JXA 8530F in the Mineral Sciences Department of the Smithsonian Institute National Museum of Natural History. A 15-keV electron beam at 10 nA with a 3- or 5-μm diameter beam was used to analyze matrix glass. Reported compositions are from single spot analyses and a secondary standard was used (Table S2 in supplementary information). In order to compare matrix glass results between the two electron microprobes, pyroclast 401LSAS9

was run on both. Replication of analyses between electron microprobes required using a log-linear fit to the time dependent intensity correction for the JEOL-JXA 8530F. For both electron microprobes, groundmass glass and plagioclase analyses with oxide totals outside 97.5–101.5 were excluded from the results.

Results

Componentry

The relative proportion of LSA, HSA, intermediate andesite, and banded andesite components varies between
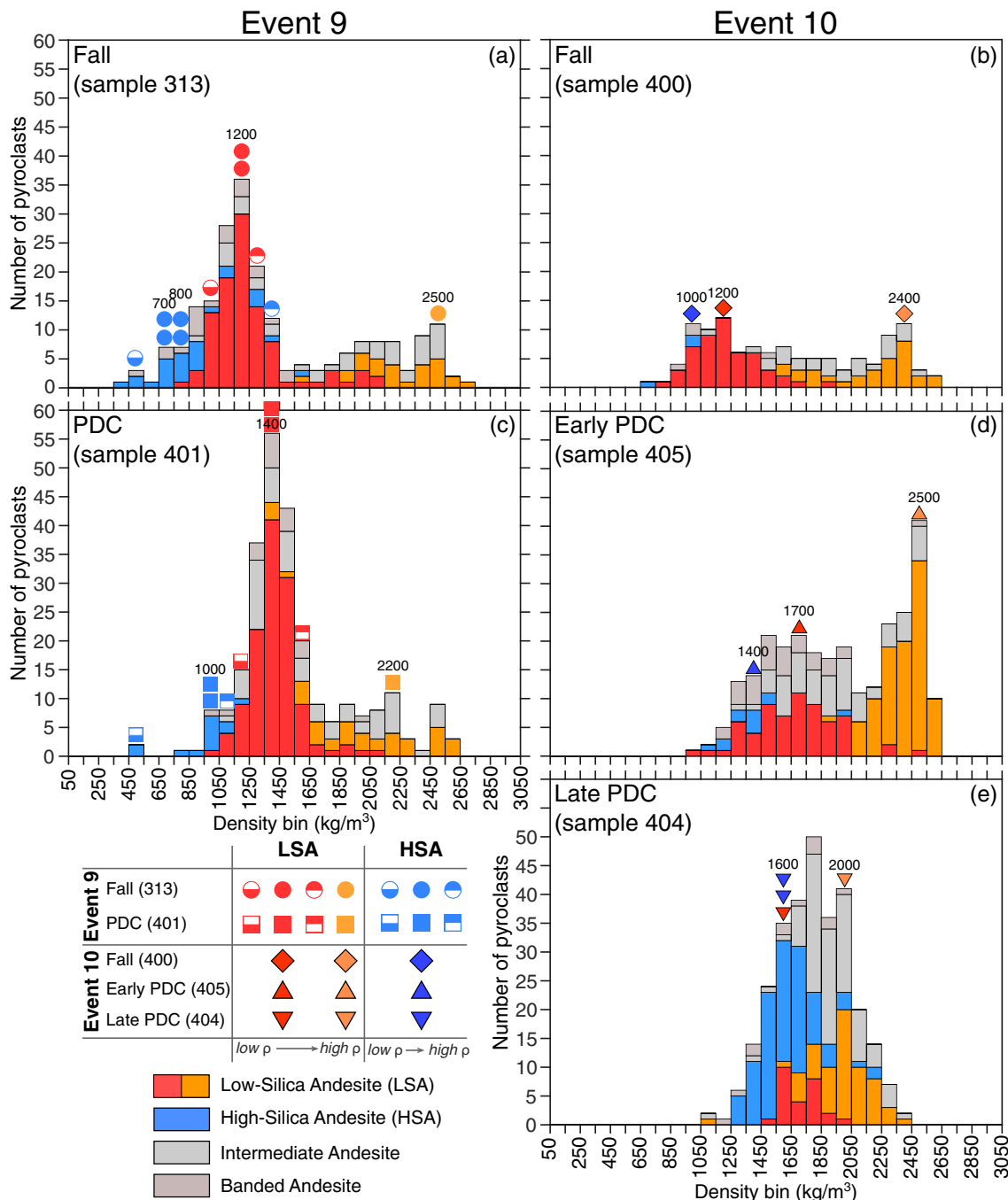
Fig. 4 Event 9 (left column) and event 10 (right column) density histograms of 16–32 mm pyroclasts by sample type and location (e.g., Fall (sample 313)). Symbols above the histogram indicate LSA scoria, dense LSA, and HSA pyroclasts selected from the mode (filled) or tail (half-filled symbols; LSA scoria and HSA only) of the density distribution for textural and chemical analysis. Symbols in the legend are arranged from low density, ρ, to high density where symbols for low-density tails have the bottom-half of the symbol filled and symbols for high-density tails have the top-half of the symbol filled. Values above symbols are the average peak value at the center of the 100 kg/m^3 density bin. The symbols and color schemes are used consistently in the following figures

eruptive events and between eruptive phases (Fig. 2). The mass percentage of LSA remained at or above 49% through most of the explosive phase of the eruption. Event 9 and the early event 10 deposits have mass fractions of LSA > 49%; however, late event 10 PDC deposit has a sharp drop in the proportion of LSA to < 50% and HSA increases to > 20%. Deposits from the continuous and effusive phases contain > 50% LSA and < 20% HSA (Fig. 2). This general pattern is consistent with previously published values although specific proportions differ, as Vallance et al. (2010) found for the 8 mm size fraction a higher percentage of LSA for events 3–8 (72% versus our 49%) and during the effusive phase (85% versus our 30%). These variations in proportions are likely a combination of different analyzed size fractions, true variability within single deposits, mass fraction versus pyroclast point counts, and that visual sorting into components is subjective.

Pyroclast density

Pyroclast densities range from 440 to 2890 kg/m^3 for all studied deposits of the 2006 eruption (Fig. 3 and Table S1 in supplementary information). For the 17 samples that span the entire eruptive sequence, deposits from the explosive phase generally have a bimodal density distribution and deposits from the continuous and effusive phase have a unimodal density distribution (Fig. 3). For events 9 and 10, we observe a similar overall range of densities, 444 to 2660 kg/m^3, with distinct differences observed between fall and PDC deposits from the same explosion (Fig. 4(a–d)), among compositional components of the same deposit (Fig. 4(a–e)), and among different PDC deposits from the same event (Fig. 4(d, e)).

Event 9

Event 9 samples from both fall and PDC deposits exhibit weak bimodal density distributions with strong modes at fairly low densities (1200 and 1400 g/cm^3) and smaller modes at higher densities (2500 and 2200 kg/m^3; Fig. 4(a, c)). Event 9 deposits are dominated by LSA scoria pyroclasts. High-silica andesite pyroclasts form a unimodal density distribution and skew towards the low density peak of the cumulative bimodal density distribution, whereas LSA (scoria and dense) and the intermediate and banded andesite compositions form two distinct modes.

Whereas both fall and PDC samples from event 9 are dominated by low-density pyroclasts, fall samples have lower mode densities overall than PDC samples (1200 versus 1400 kg/m^3). This is also true for both LSA scoria and HSA compositions where tephra fall and PDC modal densities are 1200 kg/m^3 and 1400 kg/m^3, respectively for LSA, and 700–800 kg/m^3 and 1000 kg/m^3, respectively for HSA (Fig. 4(a, c)).

Event 10

Similar to event 9, event 10–13 tephra fall and early event 10 PDC samples have bimodal density distributions (Fig. 4(b, d)). Based on the bimodal density distribution, similar proportion of LSA and HSA, and similar textures we assume event 10–13 tephra fall deposit is dominated by products of early event 10. Density modes for LSA scoria and dense LSA from event 10–13 fall sample are subequal at 1200 and 2400 kg/m^3, respectively (Fig. 4(b)). The density modes are broadly similar to the event 9 fall modes, though LSA scoria and dense LSA modes are not subequal. Early event 10 PDC density modes are 1700 for LSA scoria and 2500 kg/m^3 for dense LSA (Fig. 4(d)), which is denser than event 9 PDC (Fig. 4(c)). High-silica andesite pyroclasts in event 10–13 fall and early event 10 PDC samples are volumetrically minor and are all low density, similar to event 9.

The density distribution shifts towards a strong unimodal distribution during the later PDC of event 10 and contains a much higher fraction of HSA (Fig. 4(e)). The density mode for LSA scoria is 1600 kg/m^3 and for dense LSA is 2000 kg/m^3. The density mode for HSA is 1600 kg/m^3. As with event 9, the LSA scoria and HSA mode of event 10–13 fall is lower than the respective modes for the two PDC deposits. Though late event 10 PDC has a unimodal distribution, the density mode for LSA scoria and HSA is similar to early event 10 PDC but the mode for dense LSA is lower (Fig. 4(d, e)).

Event 9 vesicle number densities

By compositional category, event 9 pyroclasts from the fall deposit have higher VN$_V$ than pyroclasts from the PDC deposit (Table 1 and Fig. 5). For HSA, the event 9 fall pyroclast has a VN$_V$ of 1.6×10^7 mm^{-3} whereas the PDC pyroclast has a lower VN$_V$ of 4.1×10^6 mm^{-3}. For LSA scoria, VN$_V$ are overall lower than HSA for both fall, 3.1×10^6 mm^{-3}, and PDC, 1.9×10^6 mm^{-3}.

Microlite number density and crystallinity

Pyroclasts from events 9 and 10 show broad ranges of plagioclase microlite number density, MN$_V$, $10^{(4.6-6.7)}$ mm^{-3}, and microlite crystallinities, ϕ, 0.02 to 0.39 (Figs. 6 and 7). Although crystallinities of some LSA and HSA pyroclasts overlap, overall LSA trends to higher and HSA to lower crystallinities, consistent with previous qualitative observations (Larsen et al. 2010). LSA pyroclasts have plagioclase MN$_V$ of $10^{(5.5-6.7)}$ mm^{-3} and ϕ of 0.16–0.39. High-silica andesite pyroclasts have plagioclase MN$_V$ of $10^{(4.6-6.2)}$ mm^{-3} and ϕ of 0.02–0.24. We find that plagioclase MN$_V$ and ϕ of low- and high-density tails for pyroclasts from event 9 are more variable, with MN$_V$ of $10^{(5.5-6.4)}$ mm^{-3} and ϕ of 0.18–0.28 for LSA and MN$_V$ of $10^{(4.6-6.2)}$ mm^{-3} and ϕ of 0.01–0.35 for
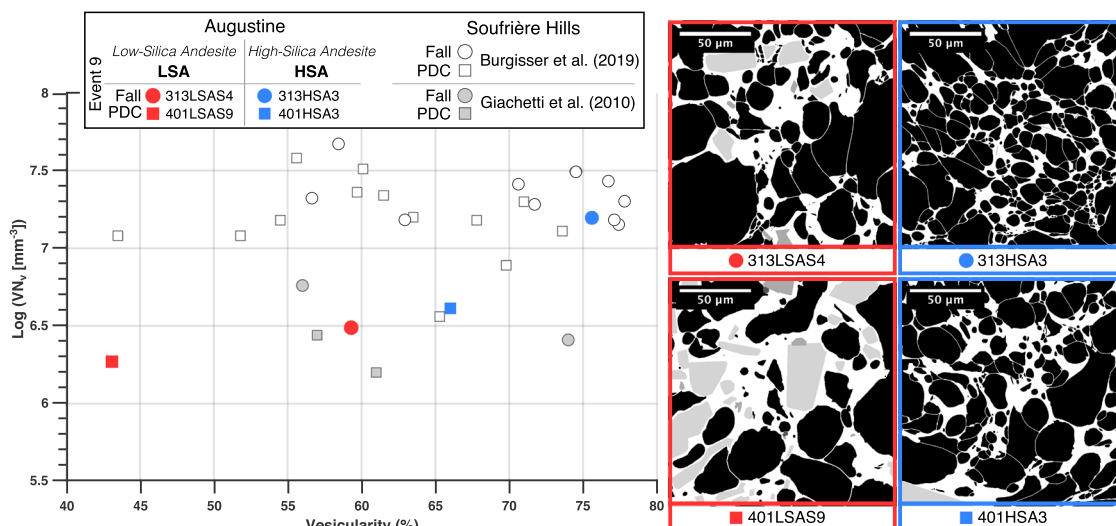
Fig. 5 Vesicle number density (VN$_V$) versus vesicularity of four pyroclasts from Augustine Volcano event 9 explosion. Red symbols are LSA scoria and blue symbols are HSA. Included for comparison are additional VN$_V$ data from two vulcanian explosions in 1997 from Soufrière Hills Volcano (Giachetti et al. 2010) and a single vulcanian explosion in 2010 from Soufrière Hills Volcano (Burgisser et al. 2019). On the right-hand side are example grayscale images digitized from BSE SEM images to calculate vesicle abundance

HSA (Fig. 6). Microlite MN$_V$ generally increase from event 9 to early event 10 and are highest within pyroclasts from late event 10 PDC. In contrast, there is no consistent change in crystallinity with time.

Pyroclasts from event 9 to late event 10 vary in groundmass texture in two additional ways: (1) the presence of a silica phase in three HSA pyroclasts (one a high-density-tail) and all dense LSA pyroclasts and (2) the abundance of broken
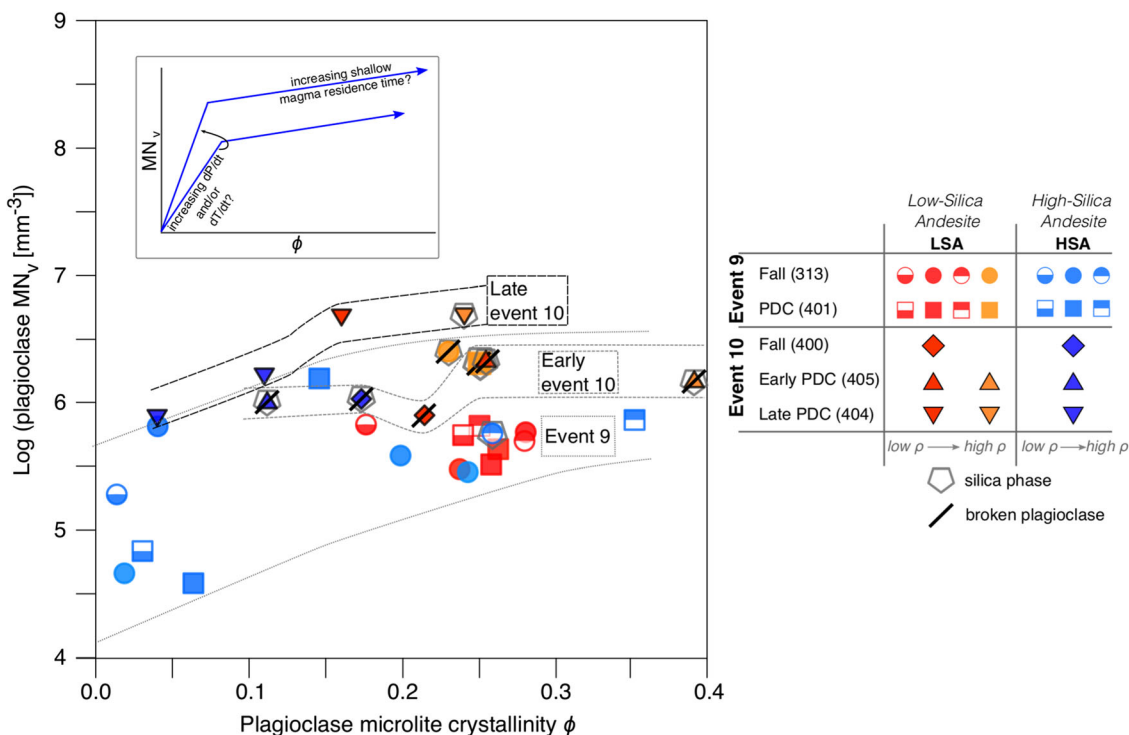
Fig. 6 Plagioclase microlite number density (MN$_V$) versus crystallinity for LSA and HSA pyroclasts. Generally MN$_V$ increases from event 9 to late event 10. Additional textures found in thin section are denoted with pentagon (silica phase) and angled line (broken plagioclase phenocrysts) symbols. Inset cartoon is a simplified illustration of previous experimental and textural work (e.g., Cashman and McConnell 2005; Clarke et al. 2007; Couch et al. 2003; Hammer and Rutherford 2002; Martel and Schmidt 2003; Miwa et al. 2009; Shea and Hammer 2013; Wright et al. 2007) where MN$_V$ increases with increasing decompression (dP/dt) or temperature (dT/dt) rates and crystallinity increases with duration of shallow storage
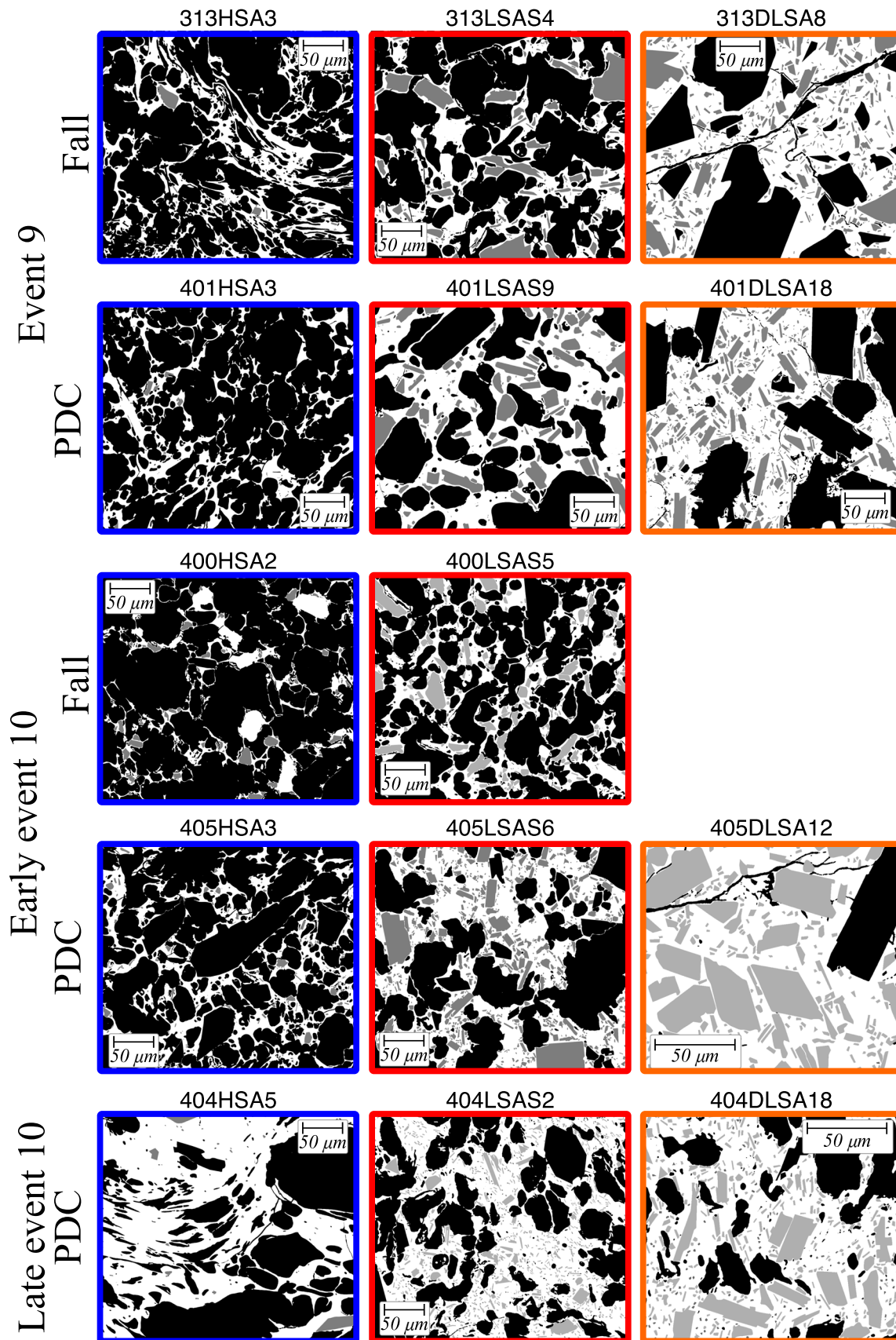
◀ **Fig. 7** Digitized BSE SEM images with hand-traced plagioclase microlites in gray, groundmass glass in white, and vesicles, excluded phenocrysts, and excluded broken plagioclase in black. Rows correspond to deposit type from eruptive events and columns correspond to high-silica andesite (HSA; blue outline), low-silica andesite scoria (LSA scoria; red outline), and dense low-silica andesite (dense LSA; orange outline)

crystals in two HSA and five LSA pyroclasts (Fig. 6). All dense LSA pyroclasts contain variable amounts of amorphous silica phase (inferred by the lack of crystalline habit in BSE-SEM images), in the groundmass. Euhedral silica phase (inferred by crystalline habit in BSE-SEM images) is present in the groundmass of one high-density-tail HSA from event 9 (Fig. S1 in supplementary information). Amorphous silica phases are present in HSA pyroclasts from the early phase of event 10 (Fig. S1 in supplementary information). The groundmass of event 10 pyroclast 400DLSA6 is sufficiently devitrified that glass analysis or microlite crystal counts were not possible. LSA and HSA pyroclasts with ϕ above 0.10 or MN_V above $10^{5.9}$ mm^{-3} are more likely to contain clearly broken plagioclase phenocrysts crystals that are < 50 μm (Fig. 6), based on truncation of concentric chemical zones (Fig. S1 in supplementary information). Early event 10 pyroclasts contain the most abundant broken plagioclase crystals (Table 1) in both LSA and HSA. Broken plagioclase crystals are excluded from the MN_V and ϕ calculations.

Glass and plagioclase compositions

Individual electron microprobe analyses of groundmass glass compositions are presented (Fig. 8, Table S2.1 in supplementary information) such that each pyroclast is represented by 4 to 16 compositional probe analyses. A majority of the pyroclasts have a relatively restricted range of groundmass glass compositions. Taken as a whole, LSA pyroclast groundmass glass compositions range between 64.5 and 78 wt% SiO$_2$; HSA compositions are less variable with a range between 72 and 79 wt% SiO$_2$. In general, groundmass glass K$_2$O contents increase as SiO$_2$ increases, whereas Al$_2$O$_3$, CaO, MgO, FeO, and TiO$_2$ contents decrease with increasing SiO$_2$ (Fig. 8). However, groundmass compositions of LSA and HSA are not colinear, showing that they do not represent a single liquid line of descent. Furthermore, within each LSA and HSA compositional suite the groundmass glass compositions of pyroclasts are not colinear (Fig. 8(a–d)). For example, all HSA pyroclasts do not follow a single liquid line of descent as illustrated by the early event 10 HSA samples that widely vary in K$_2$O at the highest SiO$_2$ contents (with amorphous silica; Fig. 8(b)).

Groundmass glass compositions of LSA and HSA pyroclasts vary between consecutive eruptive events (Fig. 8(b)). Groundmass glass compositions become more homogeneous through the studied eruptive sequence, from event 9, the most compositionally diverse, to early event 10 to late event 10. This change is most pronounced at the low silica end of the compositional range (minimum SiO$_2$ contents vary from 64.5 to 71 to 75 wt% SiO$_2$ for events 9, early 10, and late 10, respectively). In contrast, HSA glass compositions for event 9 and late event 10 have no clear progression in major element composition through the eruption sequence, but early event 10 HSA is the most evolved and contains the minimum and maximum wt% K$_2$O compositions (Fig. 8(b)).

Microlite and phenocryst plagioclase compositions (Fig. 9; Table S2.2 in supplementary information) overlap for event 9 and early event 10 (late event 10 PDC sample was not analyzed). Plagioclase phenocrysts range in anorthite composition from An$_{48-84}$ and An$_{44-84}$ for LSA scoria and HSA pyroclasts, respectively. Event 9 LSA scoria and HSA and early event 10 LSA scoria have similar microlite and phenocryst rim compositions of An$_{48-68}$; however, early event 10 HSA microlite and phenocryst rim composition is more albitic with An$_{20-56}$. Early event 10 fall HSA pyroclast, which has the highest groundmass K$_2$O (Fig. 8), contains the most albitic plagioclase from An$_{20-44}$ (Fig. 9).

Fe-Ti oxide compositions

Compositions of touching Fe-Ti oxide pairs in the groundmass and as inclusions in phenocrysts were analyzed and used to calculate temperature and oxygen fugacity (fO$_2$). Pairs that contained exsolution lamellae or were zoned were not analyzed, as was the case for HSA pyroclasts from PDC deposits. Thus, we present analyses of only LSA scoria pyroclasts from PDC deposits and LSA scoria and HSA pyroclasts from fall deposits. For the 42 pairs that passed the Mg/Mn partitioning test for equilibrium (Bacon and Hirschmann 1988), temperature and fO$_2$ were calculated using the geothermometer of Ghiorso and Evans (2008). Temperatures of 38 oxide pairs range from 868 to 1118 °C (Fig. 10; Table S2.3 in supplementary information), whereas 4 oxide pairs with anomalously high temperatures (> 1150 °C) were marked as outliers. Oxygen fugacity is consistently between 0.96 and 1.45 log units above the Ni-NiO buffer with one outlier at NNO + 0.58.

Fe-Ti oxide temperatures for event 9 are consistent with previously published Augustine 2006 Fe-Ti oxide data (Fig. 10; Coombs and Vazquez 2014; recalculated Larsen et al. 2010). For HSA, event 9 fall temperatures are similar to and within error of previously published HSA temperatures, 877 ± 8 °C (pyroclasts from late event 10 PDC deposit and effusive phase deposit; Coombs and Vazquez 2014). Although our results are consistent with the recalculated temperatures of Larsen et al. (2010) using the Ghiorso and Evans (2008) geothermometer, our results indicate a more reduced system, NNO + 1.4, than the published results of Larsen et al. (2010) which are based off the QUILF geothermometer (Andersen et al. 1993). Our results for HSA from event 10

fall yield higher temperatures (937 ± 13 °C) and lower fO_2 (NNO + 1.2; Table 1; Fig. 10) than event 9.

With the exception of two LSA scoria oxide pairs that overlap with HSA temperatures, LSA scoria oxides yield overall higher temperatures than HSA, ranging from 990 to 1120 °C (average 1044 ± 40 °C without the two low-T pairs) and are consistent with the recalculated temperature data of Larsen et al. (2010) who examined all eruptive phases and all lithologies except HSA (Fig. 10). Individual LSA scoria pyroclasts have substantial temperature ranges of at least 50 °C. Temperatures overlap between event 9 and early event 10; however, early event 10 pyroclasts are on average more reduced than those from event 9 (ΔNNO + 0.99 and ΔNNO + 1.25, respectively).

Discussion

Magma storage

Previous work sheds light on crustal storage and magma mixing prior to the 2006 Augustine eruption. Compositional endmembers LSA and HSA originate from at least two distinct resident magma sources (De Angelis et al. 2013) and are unrelated by simple crystal fractionation (Larsen et al. 2010). The rare occurrence of quenched mafic inclusions (51.8–57.1 wt% SiO_2) in the 2006 deposits indicates intrusion of basalt magma prior to the eruption (Steiner et al. 2012). Previously, the origin of LSA was proposed to be a hybrid magma of intruding basalt and HSA (Larsen et al. 2010). However, the prevalent tschermakitic amphibole of the intruding mafic magma is rarely found in LSA (De Angelis et al. 2013), prompting the interpretation that LSA magma likely resided in a shallow reservoir for decades prior to eruption, similar to HSA magma (De Angelis et al. 2013; Thompson 2011).

The different oxygen fugacities and temperatures of LSA and HSA (Fig. 10) provide further evidence for separate shallow reservoirs of LSA and HSA. The average LSA equilibrium temperature is 1028 ± 44 °C ($n = 26$; disregarding $n = 4 > 1150$ °C) and the average HSA equilibrium temperature from this study and Coombs and Vazquez (2014) is 897 ± 31 °C ($n = 24$). Additionally, HSA oxygen fugacity is about 0.2 log units above LSA.

Based on geophysical data and melt inclusion pressures, LSA and HSA likely originate from reactivated shallow crustal reservoirs at depths of 4–6 km (Cervelli et al. 2010; Power and Lalla 2010; Webster et al. 2010). Geophysical data constrain the top of a crustal magma body at 4 km beneath the surface based on earthquake locations (Power and Lalla 2010) and at 5 km below the surface based on a modeled geodetic deflation signal (Cervelli et al. 2010). Melt inclusions from Augustine 2006 LSA and HSA pyroclasts indicate maximum

entrapment pressures around 150 MPa (approximately 6 km) for 4.1–4.6 wt% H_2O, in agreement with geophysical depths (Webster et al. 2010). Recent phase-equilibria experiments using HSA pyroclasts from late event 10 PDC (RPpf) deposit suggest crystallization pressures of 120–170 MPa (corresponding to a storage depth of 4.6–6.6 km), temperatures of 840–870 °C consistent with event 9 oxide-pair geothermometry results (Fig. 10), and microlite and phenocryst compositions of An_{50-70} that are within the An range observed for event 9 HSA plagioclase (Fig. 9; De Angelis et al. 2020).

Heterogeneous groundmass glass composition is consistent with LSA and HSA magmas originating from separate crustal reservoirs; furthermore, the groundmass glass heterogeneity within LSA and HSA magmatic end members suggests more than two separate crustal reservoirs. The lack of a single liquid line of descent for either LSA or HSA groundmass glasses suggest that melt within each respective endmember is not related by crystallization alone but experienced different pressure-temperature histories in separate reservoirs (cf. Cashman and Edmonds 2019). For example, LSA scoria groundmass glass compositions lie along a single crystallization trend (Fig. 8(a–d)) but are not colinear with dense LSA (Fig. 8(a–d)) compositions from event 9 and early event 10. A subset of dense LSA have high-Cr whole-rock contents (De Angelis et al. 2013; Larsen et al. 2010) and a wide amphibole compositional range that may have resulted from HSA mixing with a mafic magma, whereas low-Cr dense LSA are most likely a product of more extensive degassing of a remnant LSA magma body (De Angelis et al. 2013). The lack of a single LSA liquid line of descent and bimodal Cr compositions suggest the 2006 eruption erupted multiple LSA magmas, and that degassing-induced crystallization alone did not drive melt evolution.

Additionally, HSA groundmass glass lacks a single linear compositional trend between SiO_2 and K_2O (Fig. 8(b)) pointing to eruption from more than one HSA magma body. We hypothesize that K_2O variation results from different HSA parent compositions, where low-K_2O HSA (Fig. 8(b)) could represent older shallowly stored magma or mobilized cumulate material (Larsen et al. 2010; Loewen et al. 2018). Ongoing tephra chronology of Augustine Volcano has found that incompatible element concentrations, including K_2O, increased through time over the past 7 ka (Loewen et al. 2018). Nearby Redoubt Volcano has a similar temporal progression where incompatible element concentrations increased at specific SiO_2 concentrations (Beget and Nye 1994). The explosive phase HSA 2006 eruptive products were previously found to contain trace elements, particularly LREE, similar to compositions of prehistoric Holocene lavas (Larsen et al. 2010). Larsen et al. (2010) suggested this divergence of composition from pre-2006 historical lavas could indicate some HSA is remobilized from the mid-crustal reservoir and is at

least hundreds of years old. Furthermore, Larsen et al. (2010) also found an explosive phase low-K_2O HSA pyroclast they suggest could represent older cumulate material. Experiments on 2006 HSA that replicate low-K groundmass glass show depletion can be caused by small amounts of biotite crystallization (De Angelis et al. 2020). Regardless of whether variation is a result of shallow-level crystallization or deeper source processes that appear to change through time, the presence of at least three K_2O-SiO_2 trends in groundmass glass data leads us to suggest there were multiple resident HSA reservoirs of various ages that were tapped and co-erupted in the 2006 Augustine eruption.

Heterogeneous whole rock, groundmass glass, and amphibole compositions provide evidence of multiple compositionally isolated reservoirs of LSA and HSA magma of various ages at Augustine Volcano (De Angelis et al. 2013; Larsen et al. 2006; Loewen et al. 2018; Harris 1994; Fig. 11). Building upon recent conceptual models for the 1986 (Roman et al. 2006) and 2006 eruptions (De Angelis et al. 2013; Larsen et al. 2010), physical separation of these bodies preserves compositional heterogeneity (Roman et al. 2006; De Angelis et al. 2013; Fig. 11) and prohibits homogenization of the magma through mixing within the eruptive sequence, which can occur as an eruption progresses (cf. Redoubt Volcano (Wolf and Eichelberger 1997)). The multiple magma reservoirs are proposed as a network of complex and interconnected dikes through which the heterogeneous magma ascends and continues to mix towards the vent (De Angelis et al. 2013; Roman et al. 2006; Fig. 11). Furthermore, we add that the discrete explosions of the explosive phase may have tapped different dikes that connect multiple magma reservoirs with the single shallow conduit and vent (Fig. 11).

Fig. 8 (a–d) Groundmass glass compositions of Augustine 2006 pyroclasts such that each pyroclast is represented by 4 to 16 compositional probe analyses. Error bars in each panel represent standard deviation of secondary standards. (e) Whole rock (small symbols; Larsen et al. 2010) and groundmass glass composition (this study) of 2006 pyroclasts. Note that the glass compositions cannot be the products of fractionation of a single crustal assemblage (dashed ellipses show composition space of Augustine phenocrysts). (a–e) Pyroclast 401LSAS9 (highlighted in (a)) was analyzed on both the U.S. Geological Survey (open red square) and the Smithsonian Institution (closed red square) electron microprobe. (b) Outline of groundmass glass compositions corresponding to event 9, early event 10, and late event 10, with a particular focus on the trends of modal density pyroclasts (density tail compositions are partially transparent)
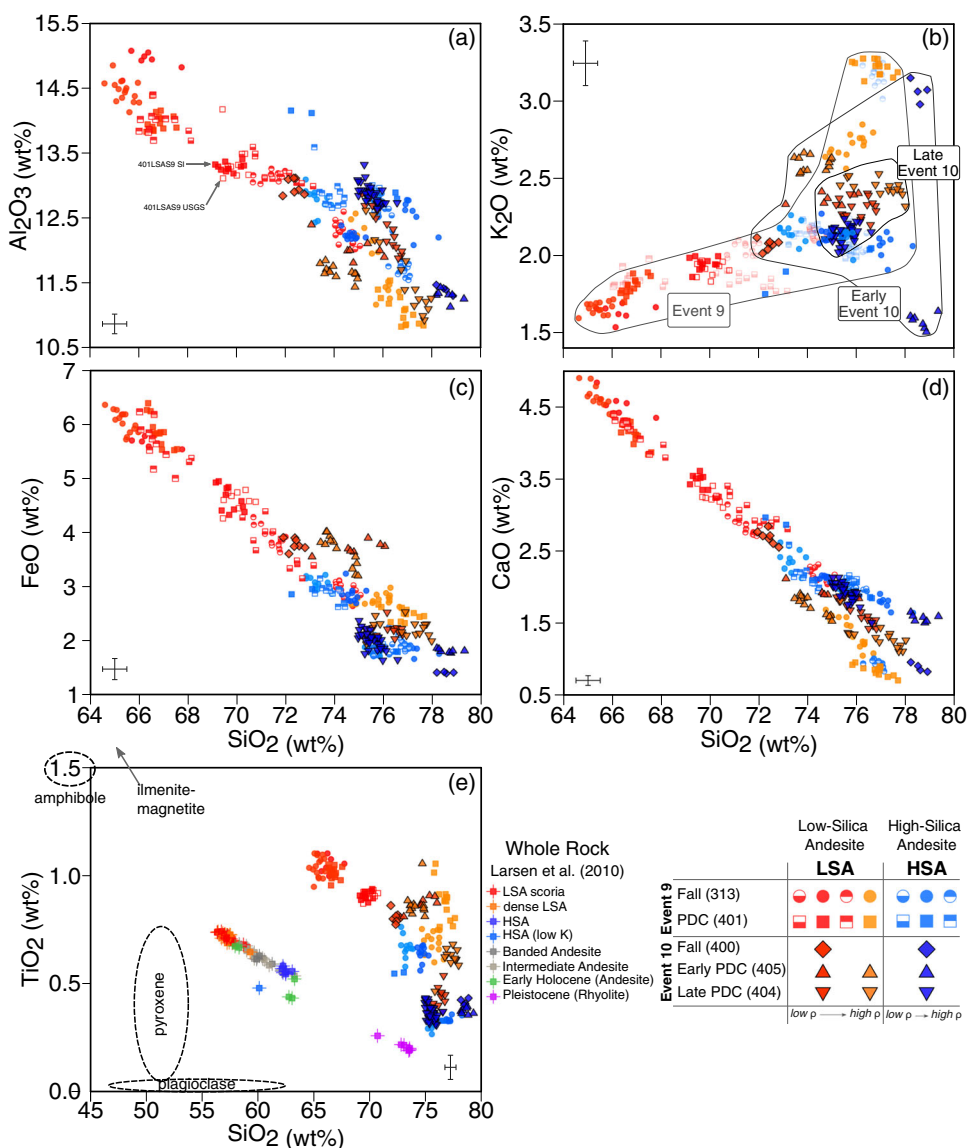
Magma staging prior to eruption

Pyroclast density distributions may provide proxies for the pre-eruptive staging depth distribution of magma prior to eruption (cf. Wright et al. 2007; we refer to all pre-eruptive magma decompression and residence above the storage zone as "staging"), and groundmass glass compositions provide information about decompression path (e.g., Blundy and Cashman 2001; Geschwind and Rutherford 1995; Hammer and Rutherford 2002). Density of event 9 and 10 pyroclasts correlates with the groundmass glass silica content (Fig. S2a in supplementary information), where denser pyroclasts are more evolved and experienced a greater degree of crystallization and gas loss (e.g., Bain et al. 2019; Cashman and Blundy 2000; Gardner et al. 1998; Wright et al. 2007). If degassing is the main driver of groundmass crystallization, then this correlation indicates that the most degassed samples have also experienced the greatest degree of outgassing. That is, the most crystalline samples represent the most degassed, shallowest (dome or shallow plug) material (Giachetti et al. 2010; Wright et al. 2007). Vulcanian or dome-forming eruptions

often have bimodal density distributions where the bimodality reflects varying degrees of pre-eruptive outgassing across a range of staging depths, and strombolian, subplinian, or phreatomagmatic eruption styles tend to produce pyroclasts with more unimodal distributions (Mueller et al. 2011).

Like other vulcanian eruptions, event 9 and early event 10 produced PDC and tephra fall deposits with bimodal density distributions (Fig. 4; discussion of differences between PDC and tephra fall density distributions from the same event is beyond the scope of this paper). Denser pyroclasts were staged near or at the surface, consistent with the presence of surface domes prior to explosions. Additionally, dense LSA and a few HSA pyroclasts have silica phase both in the groundmass or as a vapor-phase precipitate that is consistent with residence at shallow depths (e.g., Blundy and Cashman 2001; Cashman and Blundy 2000; Couch et al. 2003; Preece et al. 2016). Lower-density pyroclasts originated deeper in the conduit or upper storage system. Early event 10 has the highest proportion of dense LSA, suggesting that the relative erupted volume of outgassed magma in the dome and upper conduit was greater than in event 9. Densification of the upper conduit may have decreased permeability and inhibited efficient outgassing deeper in the conduit (Cashman and McConnell 2005; Clarke et al. 2015; Giachetti et al. 2010), which allowed degassing to build pressure beneath event 9
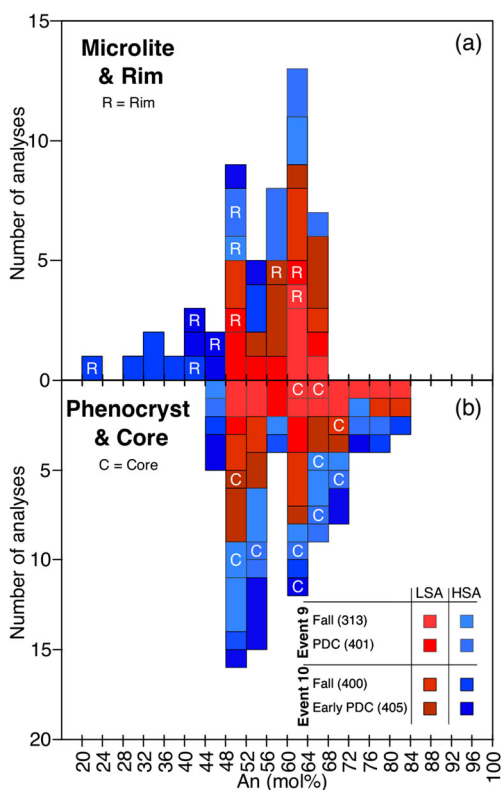
Fig. 9 Anorthite composition from electron microprobe analysis (a) plagioclase microlites and phenocryst rims with An contents ranging from $An_{20–68}$ and (b) plagioclase phenocrysts and cores with An contents ranging from $An_{44–84}$. Histogram bins are 4 An (mol%). (a) A single HSA pyroclast from sample 400 (Fall) has low An (mol%) plagioclases that are high in SiO_2, K_2O and low Al_2O_3, and also contains a silica phase and high K_2O groundmass glass. Note the colors in this figure vary slightly from the colors used for the symbols in previous figures
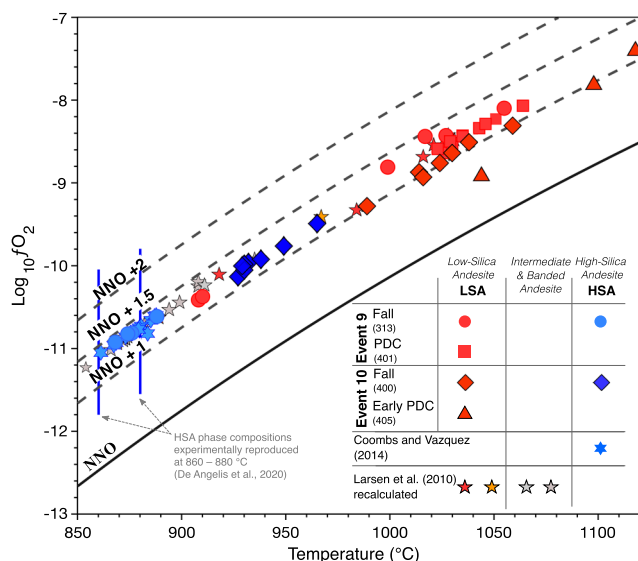
Fig. 10 Oxygen fugacity (fO_2) versus temperature for touching Fe-Ti oxide pairs from 2006 Augustine pyroclasts, as determined by the geothermometer from Ghiorso and Evans (2008). Data are from event 9 and early event 10 (this study) and previous studies of Augustine 2006 erupted products. Coombs and Vazquez (2014) pairs are from HSA pyroclasts from late event 10 PDC and the effusive phase and the pairs from Larsen et al. (2010) encompass all eruptive phases and all lithologies except HSA. Larsen et al. (2010) values are newly calculated using Ghiorso and Evans (2008) and differ from temperatures and fO_2 originally published, which were calculated using QUILF (Andersen et al. 1993). Four outlier temperature estimates for LSA (> 1150 °C) are not plotted

and event 10 domes until it overcame the structural strength of the dense cap to initiate explosion (Clarke et al. 2015).

Eruption

Vesicle number density

The use of density as a proxy for staging depth and time suggests that vesicles record syn-eruptive ascent path. We quantified VN_V for four event 9 pyroclasts and can only infer syn-eruption decompression rates for this event. LSA and HSA pyroclasts have VN_V of 10^6 to 10^7 mm^{-3}, within one order of magnitude difference, and are consistent with nucleation and growth due to similar syn-eruptive conduit decompression rates. Augustine vulcanian event 9 VN_V are similar to andesite pyroclasts from three Soufrière Hills Volcano vulcanian eruptions, two in 1997 and one in 2010 (Burgisser et al. 2019; Giachetti et al. 2010; Fig. 5). Previous calculations of Soufrière Hills VN_V correspond to decompression rates roughly between 1 and 5 MPa/s (Cassidy et al. 2018; Shea 2017). We assume based on the similar composition and VN_V that Augustine event 9 syn-eruptive decompression rates are similar.

Constraints from groundmass textures

Magma decompression and ascent history are linked with eruption style and explosivity (e.g., Cashman and McConnell 2005; Hammer et al. 2000; Scandone and Malone 1985); hence, one might expect products of similar eruptions to have similar textural characteristics. As determined by experimental studies (e.g., Brugger and Hammer 2010; Cichy et al. 2011; Couch et al. 2003; Geschwind and Rutherford 1995; Shea and Hammer 2013) and natural volcanic samples (e.g., Cashman and McConnell 2005; Hammer et al. 1999, 2000; Martel et al. 2000), plagioclase MN_V values correlate with water exsolution rate and therefore provide a proxy for magma decompression rates. For plagioclase MN_V versus microlite crystallinity, there is a clear distinction in log MN_V values between andesitic vulcanian and plinian/ subplinian eruptions such that the more explosive, faster decompression eruptions produce pyroclasts with higher MN_V values, especially at $\phi > 0.10$ (Fig. 12). Vulcanian explosions from the Augustine 2006 eruption have plagioclase MN_V values similar to those from other andesite vulcanian eruptions and are an order of magnitude or more below most products of subplinian to plinian andesite eruptions (Fig. 12).

In addition to textural differences linked to eruption style, quantitative crystallinity differences exist between HSA and LSA pyroclasts from Augustine Volcano, with HSA exhibiting overall lower values of crystallinity (Fig. 6). This is consistent with observations of Augustine 1986 and 2006 eruptive products where higher silica content pyroclasts are less crystalline (Gardner et al. 2006; Larsen et al. 2010; Roman et al. 2006). To understand what produces these textural differences between HSA and LSA, we step through two possibilities: (1) LSA and HSA experienced the same ascent histories from their respective discrete magma storage regions; therefore, there is a melt composition and/or temperature response to decompression that caused textural differences or (2) LSA and HSA experienced different ascent histories from their respective discrete magma storage regions that caused the textural differences. We assume that the late-stage, shallowest ascent history through the conduit was shared by pyroclasts that were emplaced during a single eruptive event. Here, we explore these two possibilities.

High-silica andesite versus low-silica andesite First, we focus on the role of composition and/or temperature on groundmass crystallization. Late event 10 PDC samples have the most homogeneous groundmass compositions, a unimodal density distribution (Figs. 8(b) and 3(e)), and a large erupted volume (Coombs et al. 2010), which we interpret to reflect eruption from a relatively homogeneous storage depth range (at approximately 4 km depth) with little to no inter-eruptive staging. We argue that both HSA and LSA from late event 10 PDC experienced the same decompression path because of the lack of pause between the early phase and late phase of event 10 (Coombs et al. 2010). Based upon the lower plagioclase crystallinity and slightly lower MN_V in HSA than in LSA (Fig. 6), we conclude there is a compositional and/or temperature control on plagioclase microlite crystallization in response to a single decompression path. This is consistent with experimental work that has shown viscosity and effective temperature constrain the relative rates of feldspar nucleation and growth (Hammer and Rutherford 2002), and more specifically, mafic melts have faster plagioclase growth rates than felsic melts (Hammer 2008).

Role of complex decompression history We have established that there is a compositional and/or temperature control on groundmass crystallization. However, in order to examine the additional role of decompression path, we compare the more texturally and geochemically complex products of event 9 and early event 10, which we propose had multilevel staging histories compared to the more uniform products of late event 10 (Fig. 11). First, products of event 9 and early event 10 have lower and more heterogeneous plagioclase MN_V and crystallinity than late event 10 (Fig. 6). If we use MN_V as a proxy for decompression rate (Toramaru et al. 2008), then the lower and more heterogeneous MN_V for event 9 may be the result of multiple pre-eruptive staging events before eruption (Fig. 11). We interpret the MV_V range observed in event 9 (Fig. 6) to reflect syn-eruptive withdrawal from a range of depths that had variable pre-eruptive stalling times within the conduit and variable decompression paths towards the

upper conduit. We attribute the differences between early and late event 10 pyroclasts to a lower average decompression rate for early event 10 because of pre-eruptive staging in the conduit, whereas magma decompressed more rapidly and uniformly from a storage region at depth during late event 10.

The greater range in crystallinity for event 9, 0.02–0.28, and early event 10, 0.11–0.39, products compared to late event 10 PDC, 0.04–0.24, is consistent with more widely varying P-T paths below the liquidus for a duration of days (up to 3 days repose for event 9 and 10 days repose for early event 10), during which magma decompressed and was staged in the shallow feeding system. The final distinct difference between events is the prevalence of broken crystals in early event 10 pyroclasts that we interpret to be the result of fairly rapid disruption and eruption of a brittle plug that had formed over the 10-day repose period. These variations all show that textural differences are a result of both compositional heterogeneity and decompression path before eruption (staging) and during eruption.

Groundmass glass composition and crystallinity We find that the groundmass glass composition does not correlate with plagioclase microlite crystallinity (Fig. S2b in supplementary information) as would be expected for a single decompression-induced crystallization path (cf. Mount St. Helens, Cashman and McConnell 2005). Decompression crystallization as rim growth on pre-existing crystals was not quantified here and may account for some of the lack of correlation. However, qualitatively we note that LSA pyroclasts with > 72 wt% SiO_2 in the melt do not appear to have more zoned phenocryst plagioclase than pyroclasts with < 72 wt% SiO_2 groundmass glass. We suggest the lack of consistent correlation between groundmass glass composition and microlite crystallinity indicates that melt composition and crystallization record magma evolution and decompression of multiple separate magma bodies across shallow crustal storage levels (cf. Cashman and Edmonds 2019). We note however that pyroclasts from late event 10 PDC show the most restricted range in groundmass glass composition, consistent with textural characteristics, indicating a more uniform ascent history from a more restricted pressure interval of the heterogeneous magma storage region (Figs. 6, 8(b), and 11).
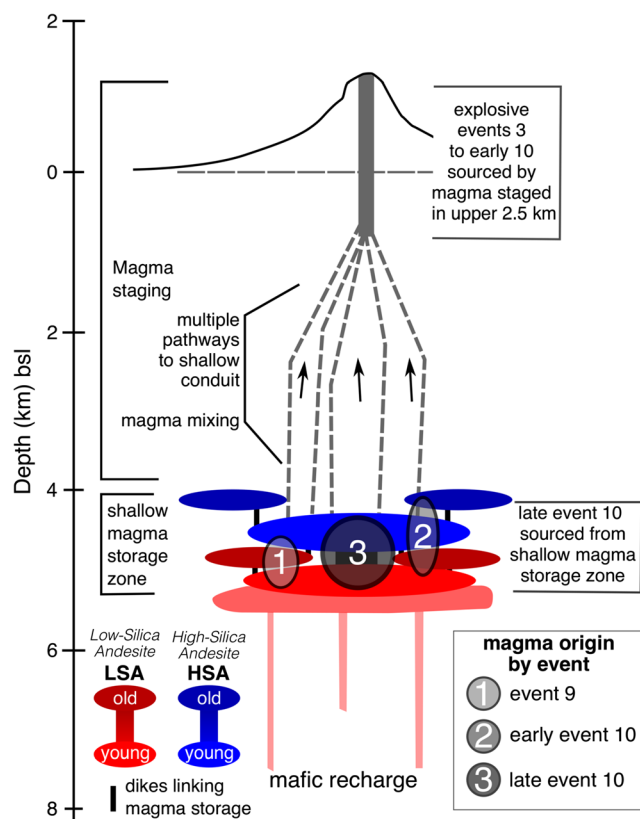
Eruption model

The geochemical and textural data presented here can be combined with previous work to reconstruct the upper-crustal magma storage and decompression processes active during events 9 and 10, and more generally, during the 2006 Augustine eruption (Fig. 11).

Six vulcanian explosions occurred on January 13–14 and erupted pyroclasts that span the andesite compositional range, producing a dense-rock-equivalent (DRE) volume of 12×10^6

m^3 (Coombs et al. 2010). If the volume of the six events is divided equally and we assume a 30-by-45 m conduit (Coombs et al. 2010), each explosion tapped an evacuation depth of < 2.5 km beneath the summit and following each explosion, magma was refilled/staged in these shallow pathways.

From January 14–17, explosions paused between events 8 and 9 when LSA, intermediate and banded andesite, and only minor amounts of HSA ascended in the conduit and effused aseismically as a smooth-surfaced lava dome. The dome was first observed on January 16 and satellite data confirm the dome actively growing up until event 9, during which time magma continued to slowly ascend. The estimated DRE volume of this dome is 2.5×10^6 m^3 (Coombs et al. 2010).

On January 17, event 9 lasted 4 min and 11 s, and produced an eruption plume up to 13.5 km asl (Webley et al. 2010) and a PDC down the southwest flank (Coombs et al. 2010; Fig. 1). Low-silica andesite dominated the products of this event, with lesser intermediate and banded andesite and minor HSA (Fig.

Fig. 11 Conceptual model of the plumbing system beneath Augustine Volcano and magma staging during the 2006 eruption. Event 9, early event 10, and late event 10 each tap different shallowly stored resident magma bodies of HSA and LSA. Shallow resident magma bodies vary in age from old to young for both HSA and LSA. Event 9 and early event 10 explosions have slightly different decompression pathways to staging magma in the upper conduit and products are erupted from the upper 2.5 km of the conduit. Late event 10 has little pre-eruptive staging and the majority of the eruptive volume is from the shallow magma storage zone. Note that the color of the various aged magma bodies does not necessarily correspond to the symbol colors used in the previous figures

2). Event 9 pyroclasts have a weak bimodal density distribution with the strongest mode at the LSA scoria range (Fig. 4). The weak mode for dense LSA likely represents fragments of the disrupted lava dome. The dominant LSA scoria mode represents andesite that resided in the conduit and/or shallow storage region and rapidly depressurized and vesiculated during the event. The impulsive and emergent acoustic waveform observed for this event (as well as the onset of event 10) can be explained as an abrupt outward acceleration of gases and volcanic material from the vent, which may be initiated by a large overpressure, followed by extended release of a pyroclast-gas mixture (McNutt et al. 2010). This is consistent with rapid disruption of the pressurized dome or plug, followed by depressurization, vesiculation, fragmentation, and eruption of the magma from deeper in the conduit. Erupted DRE volume of event 9 deposits is 8×10^5 m^3, implying evacuation of the upper 750 m of the conduit.

Event 9 textures and compositions indicate complicated upper conduit staging through multiple decompression paths. Dominant LSA exhibits a restricted crystallinity range but wider ranges in MN_V (Fig. 6) and melt composition (Fig. 8(b)) that suggest variable staging depths and decompression paths. HSA pyroclasts exhibit a wide range of microlite crystallinity, MN_V, and melt compositions (Figs. 2 and 3). This heterogeneity within both compositional end members (Fig. S2b-c in supplementary information) is because of the wide range of pre-eruptive staging depths. Such depth variation could be expected from a system with multiple shallow magma batches, where early eruptions may have triggered several pre-eruptive decompression pulses on unerupted magma below. The differences between HSA and LSA microlite crystallinities are a result of the compositional response to these complex decompression paths.

Following event 9, the volcano was relatively seismically quiet with only brief periods of drumbeat earthquakes, which are associated with lava effusion (Power and Lalla 2010). An overflight on January 24 showed no changes at the summit; however, in the last few days of January, satellite data showed a new lava dome had effused that was lighter in color and blockier than the previous dome and later sampling indicated it was also more silicic (Coombs et al. 2010).

On January 27, 2006, after a 10-day eruption repose, event 10 lasted 9 min and formed two distinct, sequential PDCs that are separated into early and late event 10 deposits (Coombs et al. 2010). Early event 10 produced pyroclasts with a bimodal density distribution, but unlike event 9, this distribution is dominated by dense LSA (Fig. 4), suggesting a higher proportion of degassed plug material relative to magma sourced from deeper within the conduit/magma storage system. Additionally, early event 10 is dominated by LSA with subordinate intermediate and banded andesite and minor HSA. Although limited observations suggest the dome was dominated by HSA composition, there are plausible explanations for the low HSA and high dense LSA proportions for early event 10. Perhaps the dome was more heterogenous than noted previously or early event 10 destroyed more of the dome that formed prior to event 9 than the smooth dome that formed before event 10. Alternatively, there may have been multiple vents and/or shallow conduits. Similar to event 9, an impulsive and emergent acoustic waveform was observed for event 10 (McNutt et al. 2010), consistent with rapid disruption of the pressurized dome or plug.

Early event 10 textures indicate a simpler eruption path than for event 9. LSA and HSA exhibit a similar range in crystallinity compared to event 9 but tend towards the higher end of MN_V. Melt compositions for early event 10 are more

Fig. 12 Plagioclase MN_V (mm^{-3}) versus crystallinity for Augustine 2006 event 9 and event 10 pyroclasts compared to plagioclase microlite data sets of andesite vulcanian to plinian eruptions from around the world. Bulk andesite compositions show a strong textural correlation to eruption style where plagioclase MN_V and crystallinity for vulcanian explosions cluster together and subplinian to plinian eruptions cluster together at higher MN_V values
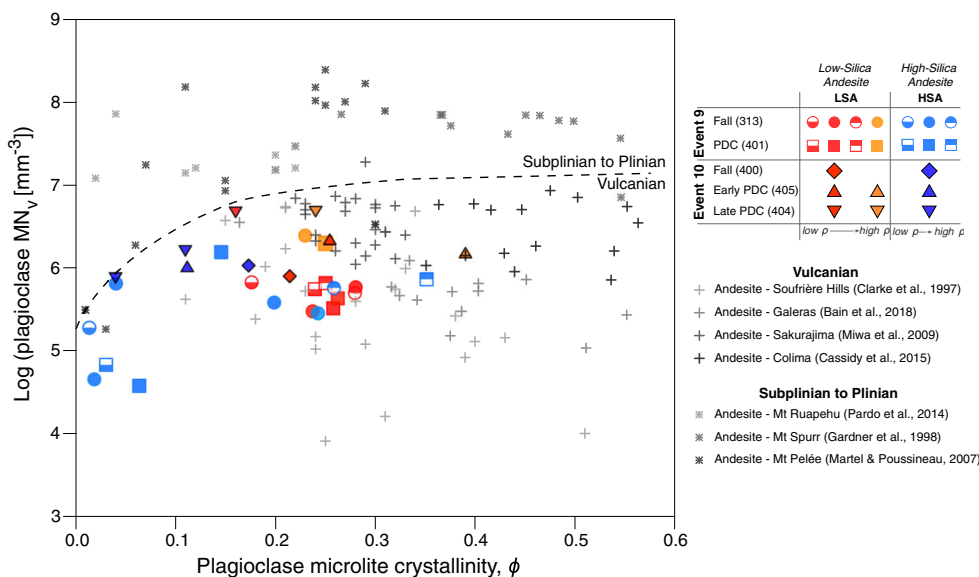
restricted in silica content than event 9 but there are at least two populations of HSA magma (in K_2O content, Fig. 8(b)). We interpret the more homogeneous MN_V values and melt compositions to indicate a simpler, syn-eruptive microlite crystallization decompression path. The longest repose interval of 10 days may have created the highest pre-eruptive overpressure of the sequence if overpressure increased through time as the shallow conduit plug continued to degas and densify. The higher abundance of broken phenocrysts in early event 10 products can be explained by the rapid depressurization of an over-pressurized system that creates sufficient strain rates to increase brittle fragmentation of melt and crystals.

During the latter part of event 10, apparently without pause, the more voluminous second PDC erupted (Coombs et al. 2010). Pyroclasts from this unit have a higher proportion of HSA and a unimodal density distribution (Figs. 2 and 3) that we interpret to reflect deeper pre-eruptive origin where low groundmass microlite crystallinities indicate there was little magma staging in the conduit. The larger DRE volume of the erupted deposits for late event 10 PDC, 1.25×10^7 m^3, supports a syn-eruptive withdrawal from magma bodies around 5 km depth and indicates a shift from explosions sourced in the shallow conduit. The relatively high MN_V suggest rapid ascent rates during this interval. We interpret that the earlier explosive events and the early phase of event 10 explosion connected the dike system beneath Augustine and provided an open pathway to eruption and rapid depressurization to tap the deeper and more homogenous LSA and HSA residual magma bodies (Fig. 11). After event 10, the Augustine system remained open and transitioned to less explosive, continuous, and effusive phases of the eruption.

Conclusions

Textural and geochemical constraints on deposits from discrete vulcanian explosive events at Augustine Volcano indicate that prior to its 2006 eruption, multiple shallow magma bodies of heterogeneous andesite resided under the volcano (Fig. 11). Low- to high-silica andesites repeatedly ascended through shallow dikes, mixing, and mingling prior to and during each vulcanian explosion. Resultant products of these vulcanian explosions are both compositionally and texturally diverse. Early vulcanian explosions, January 11–17, tapped approximately the upper 2.5 km of the staged magma beneath the volcano. Following a 10-day hiatus, January 17–27, explosive event 10, January 27, evacuated the conduit and reached deeper into the shallow storage system tapping a more homogeneous magma body dominated by high-silica andesite (HSA). This deeper tapping of magma presaged the transition from punctuated vulcanian to more continuous eruptive

behavior (Coombs et al. 2010). Our data supports an Augustine conceptual eruption model that erupts heterogeneous magma because the geometry of the system allows for multiple decompression paths and heterogeneous chemical evolution (cf. Cashman and Edmonds 2019). We propose that such an upper-crustal magmatic system is common for stratovolcanoes that erupt heterogeneous, intermediate-composition, modest-volume products in vulcanian and subplinian styles. The main conclusions and implications from our study are as follows:

- Augustine erupted multiple compositions in each explosive event by tapping multiple isolated reservoirs.
- For the Augustine system, composition affects microlite formation; thus, for the same decompression path, high-silica andesite (HSA) typically has lower microlite crystallinity compared to low-silica andesite (LSA).
- For the Augustine heterogeneous andesite system, plagioclase microlite crystallinity does not correlate with groundmass glass SiO_2 because of a variation in bulk composition between multiple shallow magma batches and pressure-temperature pathways (cf. Cashman and Edmonds 2019)
- Combining Augustine textural data with a range of other bulk andesite composition volcanoes, there exists a strong textural correlation to eruption style, where plagioclase MN_V and crystallinity for vulcanian explosions group together and subplinian to plinian eruptions group together at higher MN_V values (Fig. 12) supporting the knowledge that magma decompression rates influence eruption style (e.g., Cashman and McConnell 2005; Hammer et al. 2000; Scandone and Malone 1985).
- At Augustine, a shift from heterogeneous groundmass glass compositions to more homogeneous products correlates with an interconnection of ascent pathways within the shallow plumbing system. Pathway interconnection allowed for tapping of a larger magma body and a shift from punctuated, more closed system behavior towards open-system behavior fed by this deeper body. This change in connection led to a rapid explosive eruption (event 10) but also led to a subsequent shift to more effusive behavior as overpressure subsided.

two anonymous reviewers whose reviews significantly improved this manuscript. We thank Richard Brown and Jacopo Taddeucci for the review and editorial handling of this manuscript. Any use of trade, firm, or product names is for descriptive purposes only and does not imply endorsement by the U.S. Government.

References

Andersen DJ, Lindsley DH, Davidson PM (1993) QUILF: a pascal program to assess equilibria among FeMgMnTi oxides, pyroxenes, olivine, and quartz. Comput Geosci 19:1333–1350. https://doi.org/10.1016/0098-3004(93)90033-2

Bacon CR, Hirschmann MM (1988) Mg/Mn partitioning as a test for equilibrium between coexisting Fe-Ti oxides. Am Mineral

Bain AA, Calder ES, Cortés JA, Cortés GP, Loughlin SC (2019) Textural and geochemical constraints on andesitic plug emplacement prior to the 2004–2010 vulcanian explosions at Galeras volcano, Colombia. Bull Volcanol 81:1. https://doi.org/10.1007/s00445-018-1260-y

Befus KS, Andrews BJ (2018) Crystal nucleation and growth produced by continuous decompression of Pinatubo magma. Contrib Mineral Petrol 173:1–20. https://doi.org/10.1007/s00410-018-1519-5

Begét JE, Nye CJ (1994) Postglacial eruption history of Redoubt Volcano, Alaska. J Volcanol Geotherm Res 62:31–54. https://doi.org/10.1016/0377-0273(94)90027-2

Blundy J, Cashman KV (2001) Ascent-driven crystallisation of dacite magmas at Mount St Helens, 1980-1986. Contrib Mineral Petrol 140:631–650. https://doi.org/10.1007/s004100000219

Blundy J, Cashman KV (2005) Rapid decompression-driven crystallization recorded by melt inclusions from Mount St Helens volcano. Geology 33:793–796. https://doi.org/10.1130/G21668.1

Brugger CR, Hammer JE (2010) Crystallization Kinetics in Continuous Decompression Experiments: Implications for Interpreting Natural Magma Ascent Processes 51:1941–1965. https://doi.org/10.1093/petrology/egq044

Burgisser A, Bechon T, Chevalier L, Collombet M, Arbaret L, Forien M (2019) Conduit processes during the February 11, 2010 Vulcanian eruption of Soufrière Hills, Montserrat. J Volcanol Geotherm Res 373:23–35. https://doi.org/10.1016/j.jvolgeores.2019.01.020

Cashman K V. (2004) Volatile controls on magma ascent and eruption. In: Sparks RSJ, Hawkesworth CJ (eds) The state of the planet: frontiers and challenges in geophysics. pp 109–124

Cashman KV, Blundy J (2000) Degassing and crystallization of ascending andesite and dacite. Philos Trans R Soc A Math Phys Eng Sci 358:1487–1513. https://doi.org/10.1098/rsta.2000.0600

Cashman KV, Edmonds M (2019) Mafic glass compositions: a record of magma storage conditions, mixing and ascent. Philos Trans R Soc A Math Phys Eng Sci 377:20180004. https://doi.org/10.1098/rsta.2018.0004

Cashman KV, McConnell SM (2005) Multiple levels of magma storage during the 1980 summer eruptions of Mount St. Helens, WA. Bull Volcanol 68:57–75. https://doi.org/10.1007/s00445-005-0422-x

Cassidy M, Cole PD, Hicks KE, Varley NR, Peters N, Lerner AH (2015) Rapid and slow: varying magma ascent rates as a mechanism for Vulcanian explosions. Earth Planet Sci Lett 420:73–84. https://doi.org/10.1016/j.epsl.2015.03.025

Cassidy M, Manga M, Cashman KV, Bachmann O (2018) Controls on explosive-effusive volcanic eruption styles. Nat Commun 9:2839. https://doi.org/10.1038/s41467-018-05293-3

Cervelli PF, Fournier TJ, Freymueller JT et al (2010) Geodetic constraints on magma movement and withdrawal during the 2006 eruption of Augustine Volcano. In: Power JA, Coombs ML, Freymueller JT (eds) The 2006 eruption of Augustine Volcano, Alaska: U.S. Geol

Surv Prof Pap 1769:453–465 https://pubs.usgs.gov/pp/1769/chapters/p1769_chapter17.pdf

Cichy SB, Botcharnikov RE, Holtz F, Behrens H (2011) Vesiculation and microlite crystallization induced by decompression: a case study of the 1991-1995 Mt Unzen eruption (Japan). J Petrol 52:1469–1492. https://doi.org/10.1093/petrology/egq072

Clarke AB, Esposti Ongaro T, Belousov A et al (2015) Vulcanian eruptions. In: Sigurdsson H, Houghton B, McNutt SR et al (eds) The encyclopedia of volcanoes. Elsevier Inc., Second, pp 505–518

Clarke AB, Stephens S, Teasdale R, Sparks RSJ, Diller K (2007) Petrologic constraints on the decompression history of magma prior to Vulcanian explosions at the Soufrière Hills volcano, Montserrat. J Volcanol Geotherm Res 161:261–274. https://doi.org/10.1016/j.jvolgeores.2006.11.007

Cluzel N, Laporte D, Provost A, Kannewischer I (2008) Kinetics of heterogeneous bubble nucleation in rhyolitic melts: implications for the number density of bubbles in volcanic conduits and for pumice textures. Contrib Mineral Petrol 156:745–763. https://doi.org/10.1007/s00410-008-0313-1

Coombs ML, Bull KF, Vallance JW et al (2010) Timing, distribution and volume of proximal products of the 2006 eruption of Augustine Volcano. In: Power JA, Coombs ML, Freymueller JT (eds) The 2006 Eruption of Augustine Volcano, Alaska, U.S. Geol Surv Prof Pap 1769:145–185 https://pubs.usgs.gov/pp/1769/chapters/p1769_chapter08

Coombs ML, Eichelberger JC, Rutherford MJ (2000) Magma storage and mixing conditions for the 1953 ± 1974 eruptions of Southwest Trident volcano, Katmai National Park, Alaska. Contrib Mineral Petrol 140:99–118. https://doi.org/10.1007/s004100000166

Coombs ML, Sisson TW, Bleick HA, Henton SM, Nye CJ, Payne AL, Cameron CE, Larsen JF, Wallace KL, Bull KF (2013) Andesites of the 2009 eruption of Redoubt Volcano, Alaska. J Volcanol Geotherm Res 259:349–372. https://doi.org/10.1016/J.JVOLGEORES.2012.01.002

Coombs ML, Vazquez JA (2014) Cogenetic late Pleistocene rhyolite and cumulate diorites from Augustine volcano revealed by SIMS 238U-230Th dating of zircon, and implications for silicic magma generation by extraction from mush. Geochem Geophys Geosyst 15:4846–4865. https://doi.org/10.1002/2014GC005589

Couch S, Sparks RSJ, Carroll MR (2003) The kinetics of degassing-induced crystallization at Soufriere Hills Volcano, Montserrat. J Petrol 44:1477–1502. https://doi.org/10.1093/petrology/44.8.1477

De Angelis SH, Larsen J, Coombs ML (2013) Pre-eruptive magmatic conditions at Augustine Volcano, Alaska, 2006: evidence from amphibole geochemistry and textures. J Petrol 54:1939–1961. https://doi.org/10.1093/petrology/egt037

De Angelis SH, Larsen JF, Coombs ML et al (2020) Phase equilibrium of a high-SiO2 andesite at fO2 = RRO: implications for Augustine Volcano and other high- fO2 arc andesites. Contrib Mineral Petrol 175:1–20. https://doi.org/10.1007/s00410-020-1663-6

Degruyter W, Bachmann O, Burgisser A, Manga M (2012) The effects of outgassing on the transition between effusive and explosive silicic eruptions. Earth Planet Sci Lett 349–350:161–170. https://doi.org/10.1016/j.epsl.2012.06.056

Edmonds M, Woods AW (2018) Exsolved volatiles in magma reservoirs. J Volcanol Geotherm Res 368:13–30. https://doi.org/10.1016/j.jvolgeores.2018.10.018

Gardner CA, Cashman KV, Neal CA (1998) Tephra-fall deposits from the 1992 eruption of Crater Peak, Alaska: implications of clast textures for eruptive processes. Bull Volcanol 59:537–555. https://doi.org/10.1007/s004450050208

Geschwind CH, Rutherford MJ (1995) Crystallization of microlites during magma ascent: the fluid mechanics of 1980-1986 eruptions at Mount St Helens. Bull Volcanol 57:356–370. https://doi.org/10.1007/BF00301293

Ghiorso MS, Evans BW (2008) Thermodynamics of rhombohedral oxide solid solutions and a revision of the Fe-Ti two-oxide geothermometer and oxygen-barometer. Am J Sci 308:957–1039. https://doi.org/10.2475/09.2008.01

Giachetti T, Druitt TH, Burgisser A, Arbaret L, Galven C (2010) Bubble nucleation, growth and coalescence during the 1997 Vulcanian explosions of Soufrière Hills Volcano, Montserrat. J Volcanol Geotherm Res 193:215–231. https://doi.org/10.1016/j.jvolgeores.2010.04.001

Hammer JE (2008) Experimental studies of the kinetics and energetics of magma crystallization. Rev Mineral Geochem 69:9–59. https://doi.org/10.2138/rmg.2008.69.2

Hammer JE, Cashman KV, Hoblitt RP, Newman S (1999) Degassing and microlite crystallization during pre-climactic events of the 1991 eruption of Mt. Pinatubo, Philippines. Bull Volcanol 60:355–380. https://doi.org/10.1007/s004450050238

Hammer JE, Cashman KV, Voight B (2000) Magmatic processes revealed by textural and compositional trends in Merapi dome lavas. J Volcanol Geotherm Res 100:165–192. https://doi.org/10.1016/S0377-0273(00)00136-0

Hammer JE, Rutherford MJ (2002) An experimental study of the kinetics of decompression-induced crystallization in silicic melt. J Geophys Res Solid Earth 107:1–24. https://doi.org/10.1029/2001JB000281

Harris GW (1994) The petrology and petrography of lava from the 1986 eruption of Augustine volcano: University of Alaska Fairbanks unpublished M.S. thesis, Fairbanks, AK, 131 p

Higgins MD (2000) Measurement of crystal size distributions. Am Mineral 85:1105–1116. https://doi.org/10.2138/am-2000-8-901

Houghton B, Wilson C (1989) A vesicularity index for pyroclastic deposits. Bull Volcanol 51:451–462. https://doi.org/10.1007/BF01078811

Humphreys MCS, Edmonds M, Christopher T, Hards V (2010) Magma hybridisation and diffusive exchange recorded in heterogeneous glasses from Soufrière Hills Volcano, Montserrat. Geophys Res Lett 37:1–6. https://doi.org/10.1029/2009GL041926

Jaupart C, Allègre CJ (1991) Gas content, eruption rate and instabilities of eruption regime in silicic volcanoes. Earth Planet Sci Lett 102:413–429. https://doi.org/10.1016/0012-821X(91)90032-D

Kirkpatrick RJ (1981) Kinetics of crystallization of igneous rocks. Rev Mineral Geochem 8:321–397

Klug C, Cashman KV (1994) Vesiculation of May 18, 1980, Mount St Helens magma. Geology 22:468–472. https://doi.org/10.1130/0091-7613(1994)022<0468:VOMMSH>2.3.CO;2

Klug C, Cashman KV, Bacon C (2002) Structure and physical characteristics of pumice from the climactic eruption of Mount Mazama (Crater Lake), Oregon. Bull Volcanol 64:486–501. https://doi.org/10.1007/s00445-002-0230-5

Larsen JF, Nye CJ, Coombs ML et al (2010) Petrology and geochemistry of the 2006 eruption of Augustine Volcano. In: Power JA, Coombs ML, Freymueller JT (eds) The 2006 Eruption of Augustine Volcano, Alaska, U.S. Geol Surv Prof Pap 1769:335–382 https://pubs.usgs.gov/pp/1769/chapters/p1769_chapter15

Liu EJ, Cashman KV, Rust AC (2015) Optimising shape analysis to quantify volcanic ash morphology. GeoResJ 8:14–30. https://doi.org/10.1016/j.grj.2015.09.001

Loewen M, Wallace K, Coombs ML (2018) Geochemistry of Augustine Volcano's holocene tephra record. AGU Fall Meeting Abstracts. V33D-0278

Mangan MT, Cashman KV, Newman S (1993) Vesiculation of basaltic magma during eruption. Geology 21:157–160. https://doi.org/10.1130/0091-7613(1993)021<0157:VOBMDE>2.3.CO;2

Martel C, Bourdier JL, Pichavant M, Traineau H (2000) Textures, water content and degassing of silicic andesites from recent plinian and dome-forming eruptions at mount Pelee volcano (Martinique, Lesser Antilles arc). J Volcanol Geotherm Res 96:191–206. https://doi.org/10.1016/S0377-0273(99)00147-X

Martel C, Poussineau S (2007) Diversity of eruptive styles inferred from the microlites of Mt Pelée andesite (Martinique, Lesser Antilles). J Volcanol Geotherm Res 166:233–254. https://doi.org/10.1016/j.jvolgeores.2007.08.003

Martel C, Schmidt BC (2003) Decompression experiments as an insight into ascent rates of silicic magmas. Contrib Mineral Petrol 144:397–415. https://doi.org/10.1007/s00410-002-0404-3

McNutt SR, Tytgat G, Estes SA, Stihler SD (2010) A parametric study of the January 2006 explosive eruptions of Augustine volcano, using seismic, infrasonic, and lightning data. In: Power JA, Coombs ML, Freymueller JT (eds) The 2006 Eruption of Augustine Volcano, Alaska, U.S. Geol Surv Prof Pap 1769:85–102 https://pubs.usgs.gov/pp/1769/chapters/p1769_chapter04.pdf

Melnik O, Sparks RSJ (1999) Non-linear dynamics of lava extrusion. Nature 402:37–41

Miwa T, Toramaru A, Iguchi M (2009) Correlations of volcanic ash texture with explosion earthquakes from vulcanian eruptions at Sakurajima volcano, Japan. J Volcanol Geotherm Res 184:473–486. https://doi.org/10.1016/j.jvolgeores.2009.05.012

Mueller S, Scheu B, Kueppers U, Spieler O, Richard D, Dingwell DB (2011) The porosity of pyroclasts as an indicator of volcanic explosivity. J Volcanol Geotherm Res 203:168–174. https://doi.org/10.1016/j.jvolgeores.2011.04.006

Pardo N, Cronin SJ, Wright HMN, Schipper CI, Smith I, Stewart B (2014) Pyroclast textural variation as an indicator of eruption column steadiness in andesitic Plinian eruptions at Mt. Ruapehu. Bull Volcanol 76:1–19. https://doi.org/10.1007/s00445-014-0822-x

Power JA, Lalla DJ (2010) Seismic observations of Augustine Volcano, 1970-2007. In: Power JA, Coombs ML, Freymueller JT (eds) The 2006 Eruption of Augustine Volcano, Alaska, U.S. Geol Surv Prof Pap 1769:3–40 https://pubs.usgs.gov/pp/1769/chapters/p1769_chapter01.pdf

Power JA, Nye CJ, Coombs ML, Wessels RL, Cervelli PF, Dehn J, Wallace KL, Freymueller JT, Doukas MP (2006) The reawakening of Alaska's Augustine volcano. EOS Trans Am Geophys Union 87:373. https://doi.org/10.1029/2006EO370002

Preibisch S, Saalfeld S, Tomancak P (2009) Globally optimal stitching of tiled 3D microscopic image acquisitions. Bioinformatics 25:1463–1465. https://doi.org/10.1093/bioinformatics/btp184

Preece K, Gertisser R, Barclay J, Charbonnier SJ, Komorowski JC, Herd RA (2016) Transitions between explosive and effusive phases during the cataclysmic 2010 eruption of Merapi volcano, Java, Indonesia. Bull Volcanol 78:54. https://doi.org/10.1007/s00445-016-1046-z

Riker JM, Cashman KV, Rust AC, Blundy JD (2015) Experimental constraints on plagioclase crystallization during H2O- and H2O-CO2-saturated magma decompression. J Petrol 56:1967–1998. https://doi.org/10.1093/petrology/egv059

Roman DC, Cashman KV, Gardner CA, Wallace PJ, Donovan JJ (2006) Storage and interaction of compositionally heterogeneous magmas from the 1986 eruption of Augustine Volcano, Alaska. Bull Volcanol 68:240–254. https://doi.org/10.1007/s00445-005-0003-z

Scandone R, Malone SD (1985) Magma supply, magma discharge and readjustment of the feeding system of Mount St. Helens during 1980. J Volcanol Geotherm Res 23:239–262

Schindelin J, Arganda-Carreras I, Frise E, Kaynig V, Longair M, Pietzsch T, Preibisch S, Rueden C, Saalfeld S, Schmid B, Tinevez JY, White DJ, Hartenstein V, Eliceiri K, Tomancak P, Cardona A (2012) Fiji: an open-source platform for biological-image analysis. Nat Methods 9:676–682

Shea T (2017) Bubble nucleation in magmas: a dominantly heterogeneous process? J Volcanol Geotherm Res 343:155–170

Shea T, Hammer JE (2013) Kinetics of cooling- and decompression-induced crystallization in hydrous mafic-intermediate magmas. J Volcanol Geotherm Res 260:127–145. https://doi.org/10.1016/j.jvolgeores.2013.04.018

Shea T, Houghton BF, Gurioli L, Cashman KV, Hammer JE, Hobden BJ (2010) Textural studies of vesicles in volcanic rocks: an integrated methodology. J Volcanol Geotherm Res 190:271–289. https://doi. org/10.1016/j.jvolgeores.2009.12.003

Sparks RSJ (1997) Causes and consequences of pressurisation in lava dome eruptions. Earth Planet Sci Lett 150:177–189

Steiner AR, Browne BL, Nye CJ (2012) Quenched mafic inclusions in 2200 years B.P. deposits at Augustine Volcano, Alaska. Int Geol Rev 54:1241–1270. https://doi.org/10.1080/00206814.2011. 636641

Swallow EJ, Wilson CJN, Myers ML, Wallace PJ, Collins KS, Smith EGC (2018) Evacuation of multiple magma bodies and the onset of caldera collapse in a supereruption, captured in glass and mineral compositions. Contrib Mineral Petrol 173:1–22. https://doi.org/10. 1007/s00410-018-1459-0

Taddeucci J, Pompilio M, Scarlato P (2004) Conduit processes during the July-August 2001 explosive activity of Mt. Etna (Italy): inferences from glass chemistry and crystal size distribution of ash particles. J Volcanol Geotherm Res 137:33–54. https://doi.org/10.1016/j. jvolgeores.2004.05.011

Thomas RJ, McNutt SR, Krehbiel PR, Rison W, Aulich G, Edens HE, Tytgat G, Clark E (2010) Lightning and electrical activity during the 2006 eruption of Augustine Volcano. In: Power JA, Coombs ML, Freymueller JT (eds) The 2006 Eruption of Augustine Volcano, Alaska, U.S. Geol Surv Prof Pap 1769:581–608 https:// pubs.usgs.gov/pp/1769/chapters/p1769_chapter25.pdf

Thompson J (2011) Uranium series analysis of 2006 Augustine Volcanics: an investigation into the timescales of magmatic processes. Master's Thesis, Univ Iowa. //ir.uiowa.edu/etd/1094

Toramaru A (2006) BND (bubble number density) decompression rate meter for explosive volcanic eruptions. J Volcanol Geotherm Res 154:303–316. https://doi.org/10.1016/j.jvolgeores.2006.03.027

Toramaru A (2014) On the second nucleation of bubbles in magmas under sudden decompression. Earth Planet Sci Lett 404:190–199. https://doi.org/10.1016/j.epsl.2014.07.035

Toramaru A, Noguchi S, Oyoshihara S, Tsune A (2008) MND (microlite number density) water exsolution rate meter. J Volcanol Geotherm Res 175:156–167. https://doi.org/10.1016/j.jvolgeores.2008.03.035

Vallance JW, Bull KF, Coombs ML (2010) Pyroclastic flows, lahars, and mixed avalanches generated during the 2006 eruption of Augustine Volcano. In: Power JA, Coombs ML, Freymueller JT (eds) The 2006 Eruption of Augustine Volcano, Alaska, U.S. Geol Surv Prof Pap 1769:219–267 https://pubs.usgs.gov/pp/1769/chapters/ p1769_chapter10.pdf

Waitt RB, Begét JE (2009) Volcanic processes and geology of Augustine Volcano, Alaska. US Geol Surv Prof Pap 1762:1–78

Wallace KL, Neal CA, McGimsey RG (2010) Timing, distribution, and character of tephra fall from the 2005–2006 eruption of Augustine Volcano. In: Power JA, Coombs ML, Freymueller JT (eds) The 2006 Eruption of Augustine Volcano, Alaska, U.S. Geol Surv Prof Pap 1769:187–217 https://pubs.usgs.gov/pp/1769/chapters/ p1769_chapter09

Webley PW, Dean KG, Dehn J et al (2010) Volcanic-ash dispersion modeling of the 2006 eruption of Augustine Volcano Using the Puff Model. In: Power JA, Coombs ML, Freymueller JT (eds) The 2006 Eruption of Augustine Volcano, Alaska, U.S. Geol Surv Prof Pap 1769:507–526 https://pubs.usgs.gov/pp/1769/chapters/ p1769_chapter21.pdf

Webster JD, Mandeville CW, Goldoff B et al (2010) Augustine volcano—the influence of volatile components in magmas erupted a.d. 2006 to 2,100 years before present. In: Power JA, Coombs ML, Freymueller JT (eds) The 2006 Eruption of Augustine Volcano, Alaska, U.S. Geol Surv Prof Pap 1769:383–420 https:// pubs.usgs.gov/pp/1769/chapters/p1769_chapter16.pdf

Wolf KJ, Eichelberger JC (1997) Syneruptive mixing, degassing, and crystallization at redoubt volcano, eruption of December, 1989 to may 1990. J Volcanol Geotherm Res 75:19–37. https://doi.org/10. 1016/S0377-0273(96)00055-8

Woods AW, Koyaguchi T (1994) Transitions between explosive and effusive eruptions of silicic magmas. Nature 370:641–644. https:// doi.org/10.1038/370641a0

Wright HMN, Cashman KV, Mothes PA, Hall ML, Ruiz AG, le Pennec JL (2012) Estimating rates of decompression from textures of erupted ash particles produced by 1999-2006 eruptions of Tungurahua volcano, Ecuador. Geology 40:619–622. https://doi. org/10.1130/G32948.1

Wright HMN, Cashman KV, Rosi M, Cioni R (2007) Breadcrust bombs as indicators of Vulcanian eruption dynamics at Guagua Pichincha volcano, Ecuador. Bull Volcanol 69:281–300. https://doi.org/10. 1007/s00445-006-0073-6